Engineering Failure Analysis 186 (2026) 110532

Contents lists available at ScienceDirect

Engineering Failure Analysis

journal homepage: www.elsevier.com/locate/engfailanal

Influence of fused filament fabrication process parameters on the quasi-static mechanical behaviour and failure mechanisms of 316L stainless steel☆

J. Zenzerovic *, F. Sordetti, A. Lanzutti, E. Salvati *

Polytechnic Department of Engineering and Architecture (DPIA), University of Udine, Via delle Scienze 206, 33100 Udine, Italy

ARTICLE INFO

Keywords:
Fused Filament Fabrication (FFF)
Metal additive manufacturing
316L stainless steel
Porosity
Digital Image Correlation (DIC)
Printing parameters
Static mechanical properties

ABSTRACT

The emergence of fused filament fabrication (FFF) for metal printing has introduced a cost-effective alternative to traditional fusion-based metal additive manufacturing methods. Nevertheless, the highly inhomogeneous material microstructures resulting from this manufacturing technology seriously compromise its structural integrity performance. This study comprehensively investigates the influence of six key printing parameters – nozzle temperature, bed temperature, print speed, layer thickness, infill pattern, and infill percentage – on the quasi-static mechanical performance and dimensional accuracy of a 316L stainless steel produced via FFF. 316L stainless steel was selected as the focus material due to its widespread industrial relevance and early availability in filament form. A structured design of experiments (DOE) was implemented, followed by analysis of variance (ANOVA) and signal-to-noise (S/N) ratio analysis to assess both performance and consistency. Six material responses were evaluated: yield strength, ultimate tensile strength, stress and strain at break, toughness, and dimensional accuracy. Bed temperature was the most influential parameter, with the highest temperature of 120 °C enhancing interlayer bonding and thereby improving static mechanical properties and dimensional accuracy. The highest nozzle temperature of 250 °C provided moderate improvements in static mechanical performance, while increasing print speed to 40 mm/s improved deposition quality by reducing filament residence time and limiting binder degradation. Additionally, smaller layer thickness, line-based infill pattern, and full (100 %) infill further improved static mechanical properties by minimising interlayer voids and promoting efficient stress transfer. Hardness testing was performed to provide additional insight into the material's mechanical response. Alongside, fractography and porosity analysis were carried out to characterise failure mechanisms and quantify internal defects, revealing that large printing-induced pores dominate failure and persist after sintering, directly influencing mechanical reliability. These findings provide insights into parameter-dependent trends and interlayer bonding quality, contributing to the optimisation of print conditions for enhanced mechanical reliability and reduced variability in metal FFF components.

☆ This article is part of a special issue entitled: 'ICAM 2025' published in Engineering Failure Analysis.

* Corresponding authors.
E-mail addresses: zenzerovic.jasen@spes.uniud.it (J. Zenzerovic), enrico.salvati@uniud.it (E. Salvati).

https://doi.org/10.1016/j.engfailanal.2026.110532
Received 14 November 2025; Received in revised form 22 December 2025; Accepted 2 January 2026
Available online 3 January 2026

1. Introduction

The rapid evolution of 3D printing technology has revolutionised manufacturing processes across various industries. Among the advancements, the ability to print metals has made it possible to manufacture components with complex shapes that are difficult to achieve using traditional methods [1–4]. Most methods of 3D printing metal parts require expensive initial investments [5,6]. Up until recently, 3D-printed metallic components were considered very expensive, using technologies such as powder bed fusion, binder jetting and direct energy deposition. However, recently much cheaper method of printing metals has been introduced to the market based on material extrusion [2]. This process, regarded as a promising and cost-effective route for metal additive manufacturing, is known as fused filament fabrication (FFF) [3] also known as material extrusion additive manufacturing (MEAM) [4]. Given its significantly lower cost, this option provides a budget-friendly alternative to manufacturing metal parts with complex geometries that are very difficult or impossible to achieve using classic manufacturing methods. Producing metal parts from metal filament offers notable cost advantages, particularly for low-volume manufacturing, when compared to other metal 3D printing technologies [2,7], but also mitigates safety concerns associated with loose metal powder and laser-based methods [4,8].

Metal FFF requires a three-step process: printing, debinding, and sintering. In FFF 3D printing, a composite filament, with ~90 % of the weight being metal powders and the remaining fraction consisting of a thermoplastic material, is heated to the melting temperature of the polymer binder and then extruded layer by layer to create a three-dimensional object called a *green part*. The thermoplastic fraction of the filament acts as the binder that is necessary to make stainless steel powders flow easily and is suitable for extrusion processes.

The debinding process consists of the removal of binders. This can be done using chemical methods such as solvent debinding or catalytic debinding, or through thermal debinding, which involves controlled heating to decompose the binder [9]. After the debinding process, the part is referred to as a *brown part*. An insufficient removal of the binder material can lead to the formation of defects in the brown material, such as cracks and material impurities [10].

As far as the sintering step is concerned, the *brown part* undergoes a solid-state process under a combination of temperature and pressure, which promotes bonding between metallic particles and reduces vacancies between them, producing a material that is commonly referred to as a *silver part*.

It is important to mention that during sintering and debinding processes, printed parts undergo shrinking and distortions as metal particles combine into one solid mass, thanks to the thermomechanical loads involved. Therefore, when designing FFF metal parts, it is important to account for shrinkage. In general, this shrinking is not a well-controlled phenomenon, making the dimensional accuracy one of the outstanding issues of this manufacturing method [2,11,12]. Apart from the shrinkage, residual stresses may arise as a consequence of the microstructural changes induced by sintering [13,14]. Consequently, the material's final properties are highly dependent on the quality and control of these processes.

Furthermore, the quality of the manufactured parts is strongly influenced by the effectiveness of layer adhesion during printing and the presence of interlayer pores, which are inherent to the layer-by-layer fabrication process; these are less common in fusion-based additive manufacturing methods. Improved layer adhesion can enhance the structural integrity of the green part, contributing to greater stability and more successful outcomes during the debinding and sintering processes. Therefore, care must be taken when selecting the printing process conditions. Many assumptions regarding interlayer bonding and porosity are drawn from observations in polymer-based FDM (Fused Deposition Modelling). Since the initial stage of metal FFF involves the extrusion of a metal–polymer composite filament, similar thermal and flow dynamics apply in achieving effective layer adhesion and porosity control during 3D printing stage.

The FFF 3D printing process can be effectively controlled by modifying six key printing parameters commonly recognised to impact the quality of layer adhesion, material flow and interlayer porosity. These parameters are nozzle temperature, bed temperature, print speed, layer thickness, infill pattern and infill percentage. Particularly for 316L stainless steel [11,12,15,16], as well as other metal and polymer materials [17–23]. They are also consistently emphasised by manufacturers as critical to ensuring process reliability. The identified process parameters are known to play the following roles in the manufacturing process:

- *Nozzle temperature* controls how well the filament melts and flows through the nozzle. Low temperatures may cause a lack of filament melting and weak bonding between layers. Excessive temperatures, however, can degrade the polymeric binder, leading to inconsistent flow, clogging, or residue buildup in the nozzle [18–20].
- *Bed temperature* affects the first layer adhesion and is therefore critical for a strong, stable print foundation. In FFF, inhomogeneities in the initial layers can lead to warped bottom surfaces, causing parts to tilt or distort, which compromises the precision of subsequent layer deposition and negatively affects layer adhesion quality. If the bed temperature is too low, the initial layers may warp or detach from the build surface, resulting in part instability during printing. On the contrary, higher bed temperatures can cause the filament to excessively soften, leading to deformation and inaccuracies. Furthermore, elevated bed temperatures enhance interlayer bonding by promoting better adhesion between layers before solidification, while lower temperatures can lead to faster cooling, weakening layer adhesion [20,22,23].
- *Print speed* refers to the rate at which the print head moves while extruding material. Higher print speed, while increasing productivity, may generate incomplete infill and higher porosity. Furthermore, excessive print speeds may not allow sufficient time for the extruded material to fully thermally relax, potentially increasing residual stresses during the extrusion process negatively affecting mechanical and dimensional properties [24]. On the other hand, lower print speed results in a more constant flow of material and therefore less porosity and better mechanical properties. However, slower print speeds can increase the cooling time

of each layer, which can negatively impact the strength of bonding between layers [25]. Overall, the literature reports conflicting effects of print speed on interlayer bonding.

- *Layer thickness* is a critical parameter that significantly influences the control of interlayer porosity. Thinner layers, while decreasing the size of pores between layers, increase the number of layers needed for the same part height and therefore increase the number of interlayer pores. On the other hand, thicker layers reduce the number of layers needed which decreases the number of interlayer pores but increases the size of the pores. Furthermore, by controlling layer thickness, the area of the interlayer bonding surfaces can also be controlled, influencing the strength of the final part [19,26].
- *Infill percentage* can be modified to increase the density of the part. Layer-by-layer deposition manufacturing methods bring a peculiar form of pores and gaps controlled mainly by the quality of the printing path and how well it covers the intended geometry. Due to limitations in toolpath generation, pores and gaps can form in critical areas such as corners, sharp edges, and infill-to-wall interfaces. Therefore, slight over-extrusion has been shown in some cases to close these gaps. However, over-extrusion can negatively affect print quality by introducing uneven layer height, which can cause dimensional inaccuracies.
- *Infill pattern* has shown a big influence on directional strength in FFF-manufactured materials due to layer separation. This results in anisotropy because the bonding between layers is generally weaker than within layers. Furthermore, the type of infill pattern can influence the size and position of interlayer pores, as well as the size of the bonding area between layers, which in turn influences the mechanical and dimensional properties of the final part [19].

Although previous studies have examined a broad range of printing parameters, research specifically focusing on 316L stainless steel remains limited, with many studies based on small sample sizes, making it difficult to draw conclusive insights [11,12,15,16]. The present study focuses on limited variations of printing parameters to gain insight into their role in the quasi-static mechanical performance. The investigated parameters are those listed above. Furthermore, it will be sought whether optimised printing conditions can be identified to minimise the scattering in the mechanical behaviour and thus make this material less unpredictable. Amongst the metallic materials that can be fabricated using FFF, 316L stainless steel is one of the most widespread in various industries, chemical, pharmaceutical, medical, and marine sectors – due to its high corrosion resistance, mechanical performance and biocompatibility. Additionally, 316L stainless steel is also one of the first metal materials commercially available in filament form for FFF manufacturing. Therefore, it is evidently of great importance to investigate the mechanical properties and behaviour of metals produced through FFF manufacturing, if such a material is to be employed in structural applications. For these reasons, the present study is carried out on this specific stainless steel alloy.

To analyse the effects of the selected printing parameters, a structured statistical approach was employed. This includes an overall analysis of all samples, analysis of variance (ANOVA) to identify potentially significant factors, and a robustness assessment using the signal-to-noise (S/N) ratio, which helped identify parameters that lead to more optimal and more predictable mechanical and dimensional properties of the material. Six different material responses were considered in the analysis, including yield strength, ultimate tensile strength, stress at break, strain at break, toughness and dimensional error. Mechanical testing is performed on miniaturised samples and strain evolution in the gauge area of the samples is evaluated by using digital image correlation (DIC). While DIC has been used to map strains in metal FFF 316L [16,27], this study extends its application by correlating localised strain development directly with pore types and fracture initiation events. This yields novel information on the defect origins of failure rather than general anisotropic deformation. Hardness measurements were also performed but were not included in the parameter evaluation, as they were intended for complementary analysis. In addition to the mechanical and dimensional analyses, fractography and porosity evaluation are conducted to gain a deeper understanding of the material's internal structure and failure mechanisms.

Fractography was used to examine the fracture surfaces of tested specimens, revealing the main failure modes and the role of pores or other microstructural features in the observed material failure. Porosity analysis complements this by quantifying the amount, size, and distribution of pores, providing insight into how the printing parameters influence internal defects and overall mechanical performance. Previous research on FFF 316L has focused primarily on extrusion-related defects or printing-associated pores and their influence on mechanical performance [11,28–30]. In this study, we extend the analysis by also considering gas-entrapped pores and residual sintering pores, which are more commonly discussed in the context of conventional powder metallurgy and sintering processes [31–34]. However, in the context of FFF parts, they have mostly been mentioned rather than directly observed or quantified [36], although some studies have quantified sintering pores for other metallic materials [29,30]. This integrated approach allows a clearer understanding of how the different manufacturing stages, printing, debinding, and sintering, collectively determine the final porosity and mechanical reliability of FFF 316L components.

Overall, this work provides a critical discussion on the failure mechanisms experienced in different printing conditions, and it will provide suggestions to optimise a specific material property.

2. Materials and methods

2.1. Material and manufacturing technology

A commercially available 316L stainless steel filament, meant for FFF manufacturing, was employed – *Ultrafuse* 316L Stainless Steel filament provided by BASF©. Initially, the Ultrafuse 316L filament and the printed green part consist of 90 % metallic powder and 10 % polymeric binder. After the debinding and sintering process is completed, the chemical composition of the silver part, made entirely from 316L stainless steel, is consistent with the standard composition of 316L stainless steel (wt.%): 16.0–18.0 % Chromium (Cr), 10.0–14.0 % Nickel (Ni), 2.0–3.0 % Molybdenum (Mo), ≤2.0 % Manganese (Mn), ≤1.0 % Silicon (Si), ≤0.03 % Carbon (C), ≤0.045 %

Phosphorus (P), ≤0.03 % Sulfur (S), ≤0.10 % Nitrogen (N), while the remaining percentage of the composition is Iron (Fe) [35,36].

The 3D printing stage of the manufacturing process was conducted using an Ultimaker S5 printer equipped with specialised nozzles "Ultimaker Print Core CC 0.4" and "Ultimaker Print Core DD 0.4" specifically designed for printing metallic materials and ceramic support material, respectively.

The debinding of parts was carried out using the catalytic debinding method. Catalytic debinding happens in a gaseous environment using oxalic or nitric acid, which debinds the parts by decomposing the binders. According to BASF, the catalytic debinding process is performed at 120 °C with nitric acid HNO3 > 98 %. The subsequent sintering process was carried out according to the manufacturer's recommended guidelines [37]. Sintering was done in an atmosphere with 100 % clean and dry hydrogen (dewpoint < –40 °C) or argon (dewpoint > –40 °C). Al2O3 sintering supports of 99,6% purity are recommended.

A typical sintering cycle consists of a ramp from:

1. room temperature – 5 K/min – 600 °C, hold 1 h
2. 600 °C – 5 K/min – 1380 °C, hold 3 h
3. Furnace cooling

2.2. Mechanical testing setup and sample design

Quasi-static mechanical testing was performed using a DEBEN© Microtest tensile testing system.

This electromechanical system consists of a Microtest tensile testing stage and a corresponding control unit. The tensile testing stage is equipped with a load cell capable of measuring forces of up to 5 kN and resolutions down to 0.0001 N or 0.1 mN. A photo of the employed instrument is shown in Fig. 2.1.

Samples were designed according to the dimensions and maximum force capabilities of DEBEN tensile testing stage and do not conform to a specific standard. The geometry and dimensions of the tensile test specimen are illustrated in Fig. 2.2.

Due to the small size of the test specimens, the presence of internal defects can have a proportionally larger impact on the measured mechanical response compared to larger samples. In smaller geometries, individual pores occupy a greater fraction of the cross-sectional area, which can amplify their effect on strength and failure behaviour. However, while absolute strength values may be slightly affected by sample size, the results still provide meaningful insight into the influence of printing parameters and porosity on failure mechanisms.

A random speckle pattern was applied using an airbrush and black paint to optimise Digital Image Correlation (DIC) tracking (see Fig 2.3). Before applying the pattern, samples were lightly polished to increase the contrast between the speckles and the background. The pattern quality was evaluated by measuring representative speckles, aiming to maintain an average speckle size of approximately 3–5 pixels as recommended for accurate and reliable strain measurements by DIC guidelines [38,39].

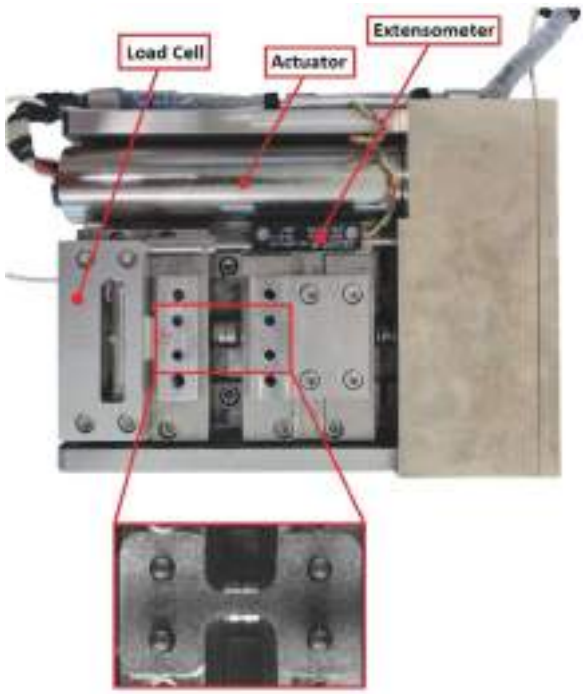

Fig. 2.1. DEBEN Microtest tensile testing stage and example of a mounted sample.

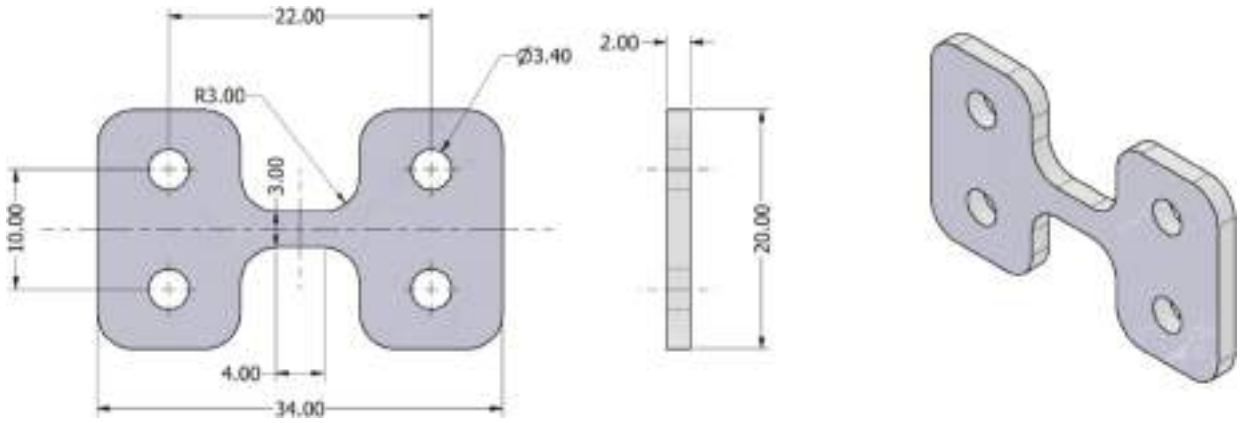

Fig. 2.2. Tensile test sample geometry and dimensions (in millimetres).

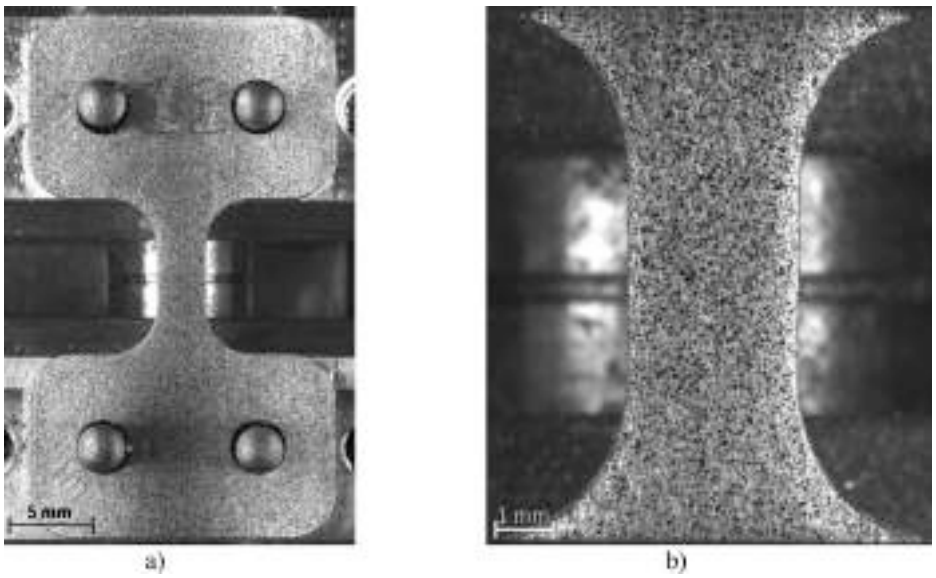

Fig. 2.3. a) sample positioned on alignment pins, b) speckle pattern.

Fig. 2.4. Complete testing setup consisting of a tensile testing machine, camera, lens and LED lights.

2.3. Digital image correlation setup and processing

To measure the strain of the tensile specimens, a customised DIC setup was used. The setup consisted of a camera, a lens and an illumination system, as shown in Fig. 2.4.

The specimens subjected to testing have rectangular shapes, which allows the strain analysis to be focused on their planar surfaces. In such a case, only small and negligible out-of-plane motions are expected. This supports the use of a simpler 2D DIC setup in contrast to a more complex and more expensive 3D (Stereo) setup.

The DIC setup utilised a Teledyne© FLIR BFS-U3-50S5M-C Blackfly S Camera, which is a monochromatic camera with square pixels as recommended for DIC applications [38]. The camera has a 5 MP (2,448 × 2,048 pixels) resolution with a pixel size of 3.45 × 3.45 μm. This ensures high spatial resolution and accurate speckle tracking with estimated field of view and speckle size. The camera features a widely used 2/3″ sensor size and it is capable of reaching a frame rate of 35 FPS. The lens used in the setup was Edmuns Optics© Techspec C Series Camera designed to be used in machine vision applications. In this study, a 50 mm fixed focal length lens was used in accordance with DIC guidelines [38,39]. The Spinnaker SDK software was utilised to customise various camera properties (e.g. frame rate, exposure time), enabling optimisation for DIC measurements.

In most cases an additional lighting is recommended for DIC applications in order to achieve good contrast with different apertures and exposure times. Good additional lighting helps to improve speckle pattern contrast and reduce image noise. The lighting system used in the setup consisted of two Phottix© M200R LED panels, one from each side of the sample to eliminate shadows and uneven illumination. Dual-side lighting improves contrast consistency across the entire sample and reduces glare, both important for accurate spackle pattern tracking. The flicker-free technology offered by the lights avoids brightness fluctuations between frames.

A Python-based DIC package (*muDIC*) was employed to evaluate the strain data from the recorded pictures. The DIC measurement grid was positioned away from sample edges and fillets to avoid boundary effects and ensure accurate strain measurement. This region of interest was kept consistent across all samples to maintain comparability.

A customised Python script was developed to synchronously acquire pictures and force and allowing for an accurate correlation between load and strain. In this way, stress–strain curves were constructed by combining strain data calculated using the "muDIC" Python scripts with force measurements recorded by the tensile testing machine's load cell.

2.4. Data analysis methods

To perform the analysis of the tensile test data and evaluate the effects of the printing parameters on the mechanical properties of FFF-manufactured 316L stainless steel, this study exploited the design of experiments (DOE) approach. This allowed to systematically plan and organisation of the tests, allowing identification of the effects of various printing parameters on the measured outcomes.

A D-optimal design based on a full factorial experiment was used to reduce the number of experimental runs while preserving the ability to estimate the main effect of printing parameters while accommodating practical constraints such as time and material limitations. In this way, the experiment was reduced to a statistically powerful subset of runs and ensured an efficient coverage of the design space.

ANOVA's general linear model was used to determine statistical significance based on p-values calculated for each parameter and parameter levels. D-optimal designs are tailored to minimise parameter uncertainty by selecting a smaller, information-rich set of experimental runs. Therefore, lower R^2 values are a natural consequence of how D-optimal designs prioritise efficient parameter estimation and do not necessarily reflect poor model quality. Therefore, to assess whether the model adequately represented the data, the lack-of-fit was evaluated based on its p-value, and model quality was further examined through analysis of the four standard residual plots.

Practical significance of parameters was estimated using Cohen's d values, which is determined using mean values and standard deviations corresponding to the two parameter levels being compared. Cohen's d value is given by the following equation:

$$d = \frac{\overline{x_1} - \overline{x_2}}{s_p}$$

where $\overline{x}_1$ and $\overline{x}_2$ represent response mean values of two compared parameter levels. Spooled deviation is labelled as s_p and given with:

$$s_p = \sqrt{\frac{(n_1 - 1)s_1^2 + (n_2 - 1)s_2^2}{n_1 + n_2 - 2}}$$

where s_1 and s_2 represent standard deviations of two compared parameter levels for the observed response, while n_1 and n_2 represent the number of tested samples for each case.

Lastly, in the absence of statistically and practically significant effects, the robustness approach was used to choose parameter levels that result in the highest and most constant results, favouring high response as well as predictability of the results. In this part of the analysis Taguchi's signal-to-noise ratio was adopted as an alternative approach to perform robustness analysis and to assist in drawing meaningful conclusions. The signal-to-noise (S/N) ratio favours both improved performance and consistency by rewarding parameter levels that produce higher or lower mean responses while minimising variability, therefore promoting more robust and repeatable results.

Mechanical responses were ranked according to the larger-the-better S/N ratio equation, favouring greater values of responses,

while dimensional error responses were ranked according to the smaller-the-better S/N ratio equation, favouring parameter levels that result in smaller dimensional error. Higher S/N ratios meant better robustness. S/N ratio larger the better is given with the following equation:

$$S_N = -10\log\left(\frac{1}{n}\sum_{i=1}^{n}\frac{1}{y_i^2}\right)$$

While the smaller-the-better S/N ratio by:

$$S_N = -10\log\left(\frac{1}{n}\sum_{i=1}^{n}y_i^2\right)$$

where y_i describes response values for a certain parameter level.

To enable fair and meaningful comparison across multiple response types (e.g., yield strength, UTS, strain at break), the signal-to-noise (S/N) ratios were first normalised using min–max normalisation. This normalisation was performed within each response type and for each parameter independently, so that for a given parameter (e.g., nozzle temperature), the S/N ratios across its levels (e.g., 230 °C, 240 °C, 250 °C) were scaled to a 0–1 range within the same response.

$$S/N_{norm.} = \frac{S/N_i - S/N_{min}}{S/N_{max} - S/N_{min}}$$

where:

- S/N_i represents the original Signal-to-Noise ratio value associated with the *i*-th level of a given process parameter and a specific response (e.g., yield strength).
- S/N_{min} is the minimum S/N ratio among all levels of the same process parameter for the same response.
- S/N_{max} is the maximum S/N ratio among those same levels.
- $S/N_{norm.}$ is the resulting scaled value ranging from 0 to 1, where 0 corresponds to the least favourable level and 1 to the most favourable, within the context of the parameter and response considered

Once the normalised S/N ratios were obtained, Grey Relational Analysis (GRA) was used to combine them across the six responses for each level of a parameter. This resulted in a Grey Relational Coefficient (GRC) for each level, reflecting its overall performance across all responses.

$$GRC = \frac{\Delta i(k) + \zeta \cdot \Delta max}{\Delta min + \zeta \cdot \Delta max}$$

- $\Delta i = |1\text{-}S/Ni|$: the absolute difference between the result of your experiment and the ideal result, ideal being equal to 1 in normalised values
- Δmin and Δmax: The smallest and largest differences across all experiments and all responses. With normalised values, these are equal to 0 and 1, respectively.
- ζ: A distinguishing coefficient

The distinguishing coefficient was set to a typical value of 0.5. This coefficient adjusts the sensitivity of the analysis. It does not usually need to be changed unless you have a specific reason.

The Grey Relational Grade (GRG) is the average of all GRCs for a given parameter level.

$$GRG = \frac{1}{n}\sum_{i=1}^{n} GRC$$

This procedure was performed separately for each parameter. That is, each parameter (nozzle temperature, bed temperature, print speed, etc.) was evaluated independently, and the GRG values were used to rank the levels within that parameter, identifying the level that consistently provided stronger overall results across all considered responses.

2.5. Hardness tests

The hardness of each sample was measured using a *Zwick-Roell Durajet G5* durometer, a semi-automatic instrument capable of applying loads from 9.8 N to 2450 N. The device performs standardised hardness tests according to Rockwell scales (HRA, HRB, HRC, HRD) and Brinell tests under displacement control using indenters with diameters of 1 mm, 2.5 mm, and 5 mm. It is also suitable for testing polymeric and composite materials. The wide selection of indenters, extensive load range, and integrated software for data acquisition and export make the instrument highly versatile.

Hardness measurements were performed in the gripping section of each specimen. Care was taken to ensure that the analysed surface and its opposite face were sufficiently flat and parallel to avoid measurement errors.

2.6. Fractography

Fracture surface analyses were performed using a *ZEISS Evo 40* Scanning Electron Microscope (SEM). The instrument operates by directing a thermionically generated electron beam, accelerated through a high potential difference and focused by electromagnetic lenses, onto the specimen surface. The interaction between the electron beam and the sample produces several signals detected by dedicated sensors. Secondary electrons (SE) were used to obtain morphological information, while back-scattered electrons (BSE) provided compositional contrast. An *Oxford INCA X-Sight EDXS* detector was also employed for semi-quantitative chemical analysis through X-ray spectroscopy.

Prior to SEM observation, all fracture surfaces were cleaned in ethanol and dried.

2.7. Porosity analysis

Porosity was examined using a *Zeiss Axio Vert.A1* inverted optical microscope equipped with a *Zeiss Axiocam 208 Color* digital camera. This configuration, typical in metallographic analyses, allows the prepared surface of the specimen to face downward, ensuring focus stability with a single planar surface. The microscope is equipped with 5×, 10×, 20×, 50×, and 100 × objectives and can operate in bright-field, dark-field, and polarised light modes.

Samples were sectioned in the calibrated region using a coolant-assisted cutting wheel, embedded in epoxy resin, and subjected to standard metallographic preparation to obtain mirror-like surfaces. Under bright-field illumination, pores appeared as black areas against the bright metallic matrix, providing high contrast for subsequent image analysis.

3. Analysis

3.1. Design of experiment

Minitab© software was used to define and optimise experimental space. Initial D-design was generated using the *Sequential method* and then further improved by *Fedorov's method*.

The six key printing parameters were investigated: nozzle temperature, bed temperature, print speed, layer thickness, infill pattern and infill percentage. Available documentation shows various recommended values and ranges for these parameters. With a goal to find the parameter levels that produce parts with better and more stable specific static mechanical properties, it was decided to test these parameters in these manufacturers' recommended ranges. In this study, anisotropy in FFF-manufactured materials was not the primary focus, as its influence on directional strength due to layer separation has been well established in previous research. As part of the investigation, two different infill patterns were evaluated: a standard line pattern with alternating layers printed at ± 45°, and a cubic infill structure. The goal was to explore whether modern infill patterns like cubic orientation would influence mechanical performance in metal FFF. This study investigated the most influential printing parameters in the following ranges:

Table 3.1
Order of the experimental runs and corresponding parameter configurations.

Sample#	Nozzle Temp. [°C]	Bed Temp. [°C]	Print Speed [mm/s]	Layer Thickness [mm]	Infill Pattern	Infill Percentage [%]
1	250	120	40	0.1	Lines	100
2	230	120	40	0.15	Cubic	105
3	250	70	20	0.1	Cubic	105
4	250	90	40	0.15	Lines	105
5	240	90	40	0.1	Cubic	100
6	250	120	30	0.15	Cubic	100
7	230	70	20	0.15	Lines	100
8	240	120	30	0.1	Lines	105
9	230	90	30	0.1	Lines	100
10	230	70	30	0.1	Lines	100
11	240	70	40	0.15	Lines	100
12	240	120	20	0.15	Lines	100
13	230	90	20	0.1	Cubic	105
14	250	90	30	0.15	Lines	105
15	240	90	20	0.15	Cubic	100
16	240	120	20	0.1	Lines	105
17	250	70	40	0.1	Cubic	100
18	230	120	40	0.15	Cubic	105
19	240	70	40	0.1	Lines	105
20	250	70	20	0.15	Lines	105
21	250	120	20	0.1	Cubic	100
22	240	70	30	0.1	Cubic	105
23	230	70	30	0.15	Cubic	100
24	230	90	20	0.1	Lines	105
25	240	90	30	0.15	Cubic	105

- Nozzle temperature (230 °C–250 °C)
- Bed Temperature (70 °C–120 °C)
- Print Speed (20–40 mm/s)
- Layer Thickness (0.1, 0.15 mm)
- Infill percentage (100 %, 105 %)
- Infill pattern (lines, cubic)

This approach enabled the estimation of main effects while reducing the number of required tests to a statistically powerful subset of 25 runs or a unique combination of parameter levels. For each parameter configuration (i.e., each run), one replicate was included, meaning two samples were tested per run. By introducing replicates, the experiment accounted for random variability and helped distinguish real effects from random fluctuations. The entire experiment, therefore, consisted of 50 tests. Each run was assigned a numerical label from 1 to 25, with replicates denoted using a decimal format (e.g., 1.1 and 1.2), allowing clear identification of both the run and its corresponding replicate (see Table 3.1).

3.2. Tensile test setup specifications

Tensile tests were conducted under displacement control at a constant motor speed of 0.5 mm/min. The resulting load was continuously recorded and used, which was later used to compute stress evaluation.

DIC setup was used to evaluate strain along the sample loading direction. The frame rate was set at 1 Hz, corresponding to one image acquired per second during the tensile test. Exposure time was fixed at around 12000 μs. Gain values were kept at zero, while Gamma levels were around 0.8, which enhanced contrast in the dark areas and showed better results regarding speckle tracking. Gamma refers to the relationship between the input light intensity and the output brightness of an image. The lens aperture was fixed at f/8 for all tests, as this setting provided an appropriate depth of field and optimal image quality under the given lighting conditions and in combination with the selected camera parameters.

The previously applied speckle pattern (3–5 pixel average size) ensured reliable DIC tracking during the tensile test, providing sufficient contrast for accurate local strain measurements.

In DIC, ensuring adequate image contrast is crucial for accurate strain measurements. Recommended minimum contrast is approximately 20 % of the full dynamic range. However, 50 % (130 count) is typically preferred. For 8-bit cameras, that means approximately 50 counts, meaning 50 greyscale levels between the speckles and background. The measured speckle patterns exhibited a greyscale intensity difference of approximately 100–150 counts between speckles and the background, exceeding the minimum contrast required for reliable DIC measurements.

3.3. Responses

To assess the mechanical performance of the samples, the processed stress–strain data were used to determine key material properties: yield strength, ultimate tensile strength, stress at break, strain at break, and toughness.

Yield Strength was determined using a 0.1 % offset method with a fixed Young's modulus of 200 GPa for all samples, as inspection of stress–strain curves revealed that plastic deformation occurred before conventional 0.2 % strain.

Stress at break was identified as the point where the measured stress dropped by at least 5 MPa from the last recorded value, indicating failure. The corresponding strain at this point was recorded as the strain at break. Based on this endpoint, toughness was calculated as the area under the stress–strain curve using the trapezoidal integration method.

The accuracy of final parts is one of the outstanding issues of FFF manufacturing of metal components due to shrinkage during debinding and sintering. Therefore, to account for the dimensional error and to calculate stresses more accurately, the cross-sectional area was measured using a calliper of 0.05 mm resolution. The difference between the nominal area of 6 mm^2 and the actual measured area was recorded as "area error" and it was used as a representative of dimensional accuracy.

3.4. Statistical analysis

The determined responses were used to evaluate the overall variability in mechanical performance, assess dimensional accuracy and analyse the influence of printing parameters on each measured property.

As an initial step in the analysis, descriptive statistics were performed in Minitab© to summarise the data and gain a preliminary understanding of the central tendency, variability, and distribution of the measured mechanical responses. This step provided an overview of mean values, standard deviation and minimum and maximum values of all the tested samples.

Out of 50 printed samples, n.9 samples (batch 2) underwent debinding and sintering separately form the remaining 41 (batch 1), i.e. at a few days of distance. This was done to simultaneously capture any significant change and variability due to the repeatability of the material post-processes.

Including batch as a parameter in the analysis helped account for potential variability not related to printing parameters. To account for the batch factor, Fisher's exact test was performed to analyse the relationship between two categorical variables: batch (categorised as Batch 1) and Batch 2) and sample quality (categorised as good or defective). If a significant correlation was found, defective samples were excluded from the parameter evaluation analysis, as their occurrence was assumed to be related to factors outside the defined printing parameters.

The second part of the analysis consisted of evaluating the effects each parameter has on the measured responses. Across the 50 tests, each parameter level was tested approximately 16–18 times for parameters with three levels (nozzle temperature, bed temperature, and print speed), and 24–26 times for parameters with two levels (layer thickness, infill pattern, and infill percentage). This provided sufficient data to reliably estimate main effects and draw meaningful conclusions regarding the influence of manufacturing parameters on static material properties.

According to ANOVA's general linear model, specific parameter levels were favoured for both bed temperature and layer thickness based on their influence on the responses. Additional trends were explored through the analysis of interval plots, which provided insights and rough estimations of response behaviour across all measured parameter levels. The practical significance of each parameter was evaluated using Cohen's *d* value, calculated based on the mean values of the two response levels of the investigated parameter and their pooled standard deviation.

The final part of the statistical analysis utilised Taguchi's signal-to-noise ratio (S/N) as an alternative approach to perform robustness analysis and to assist in drawing meaningful conclusions. Mechanical properties were evaluated using the larger-the-better criterion to prioritise higher and more consistent performance, while dimensional errors were assessed using the smaller-the-better criterion to favour lower and more stable deviations. Normalisation of the signal-to-noise (S/N) ratios followed by grey relational analysis was performed to assess overall response behaviour. The results revealed clear trends and indicated a preference for specific parameter levels across the evaluated responses.

3.5. Hardness tests

Hardness testing was conducted in accordance with ASTM E18-22: *Standard Test Method for Rockwell Hardness of Metallic Materials* [40]. According to this standard, the indenter is brought into contact with the test specimen and the preliminary test force *F0* is applied. In the Rockwell hardness method, the preliminary force is 10 kg_f (98 N). After maintaining the preliminary force for the specified dwell time (1–4 s), the initial indentation depth is recorded. The force acting on the indenter is then increased by applying the additional test force *F1*, reaching the total test force *F*. For the Rockwell hardness test, the total test forces are 60 kg_f (589 N), 100 kg_f (981 N), and 150 kg_f (1471 N). This total force is held for the prescribed dwell time (2–6 s). The additional test force is subsequently released, returning the system to the preliminary test force. After maintaining the preliminary test force for the specified dwell time (2–5 s), the final indentation depth is measured. The Rockwell hardness number is determined from the difference *h* between the final and initial indentation depths, both measured under the preliminary test force. Finally, the preliminary force is removed and the indenter is withdrawn from the specimen.

For scales using a ball indenter, the Rockwell hardness is calculated as:

$$HR = 130 - h/0.002$$

In this work, the HRB scale was adopted, corresponding to a 1/16 in (1.588 mm) ball indenter and a total test force *F* of 100 kg_f (981 N).

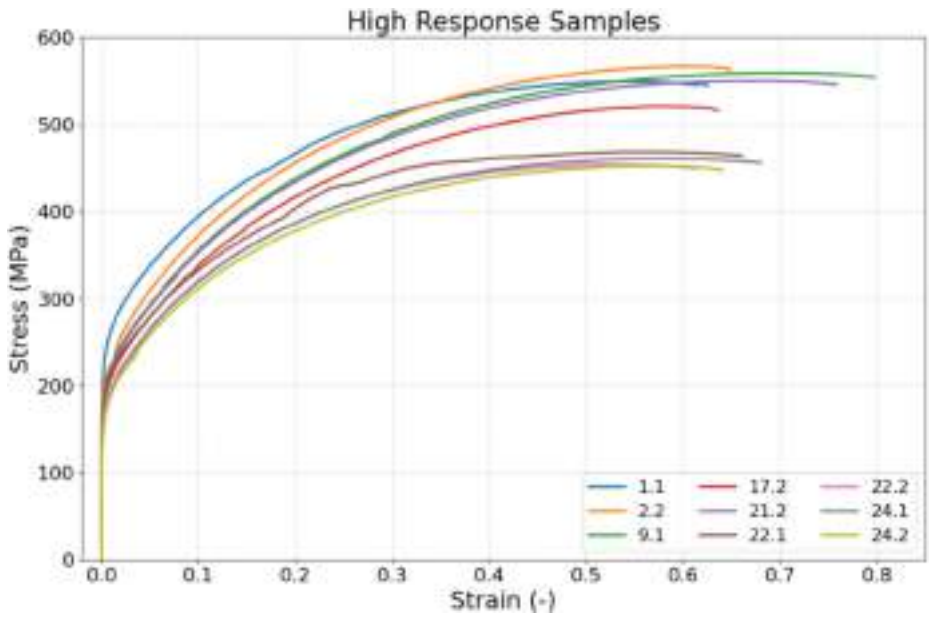

Fig. 4.1. Stress-Strain Curves of high performing samples, defined in terms of ultimate tensile strength (UTS) and strain at break.

3.6. Fractography

All fracture surfaces were examined using the SEM at different magnifications by analysing secondary electrons. Initially, low-magnification images at 50 × were acquired to capture the overall morphology of the fracture surface. After that, regions of particular interest were observed at higher magnifications of 100×, 250×, and 1000 × to investigate finer structural details.

3.7. Porosity analysis

Porosity analysis was performed to evaluate pore morphology, shape, and defect types in the examined specimens. For each specimen, multiple panoramic images were acquired at 50 × magnification to cover the entire calibrated cross-section, along with additional 100 × images focused on the central region.

The acquired micrographs were processed using *ImageJ 1.54 g* software. The true area of the sample cross-section was first determined and used as a reference for porosity calculations. Pores were then identified by applying a grayscale threshold to separate voids from the solid material. Individual pore areas were measured using the "Analyse Particles" function, and total porosity was calculated as the ratio of the sum of pore areas to the measured cross-sectional area. This approach enabled detailed characterisation of different pore types, including their size, shape, and spatial distribution within the microstructure.

4. Results

To illustrate the range of mechanical responses, representative stress–strain curves are presented, including those corresponding to the highest-performing samples, several exhibiting behaviours near the average, and those with the lowest mechanical performance, with ultimate tensile strength and strain at break as indicators of overall behaviour. Defective samples are presented separately to highlight abnormal behaviour.

Fig. 4.1 shows several samples representative of the upper range of measured mechanical performance. These samples exhibited responses above the average, with ultimate tensile strength (UTS) exceeding 450 MPa and strain at break above 0.6.

Samples showing mechanical performance around the average of the measured results are shown in Fig. 4.2, with ultimate tensile strength ranging from 400 to 450 MPa and strain at break between 0.4 and 0.55.

Samples that performed in the lower expected range are shown below in Fig. 4.3. These samples exhibited a response slightly below average in both ductility and strength, with UTS dropping below 400 MPa and strain at break below 0.4.

Samples that were identified as anomalous are shown below to demonstrate the effect of potential manufacturing anomalies on material behaviour (see Fig 4.4). These samples failed at very low strains, typically below 0.1.

4.1. Overall analysis

Initial statistical analysis of all 50 samples revealed overall trends and variability in the six measured mechanical properties — yield strength, ultimate tensile strength, stress at break, strain at break, and toughness — providing a foundation for more detailed

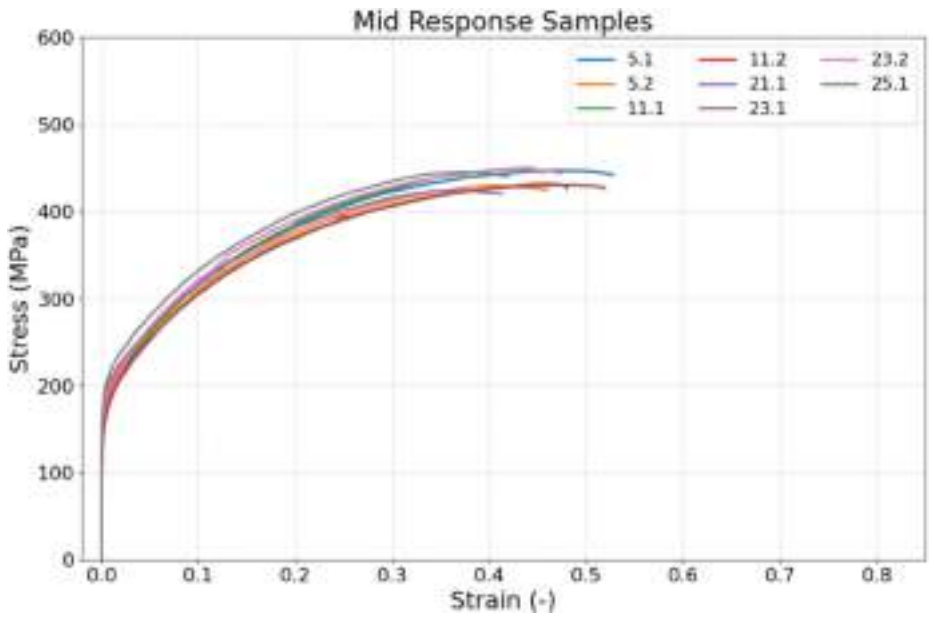

Fig. 4.2. Stress-Strain Curves of the average response sample, defined in terms of ultimate tensile strength (UTS) and strain at break.

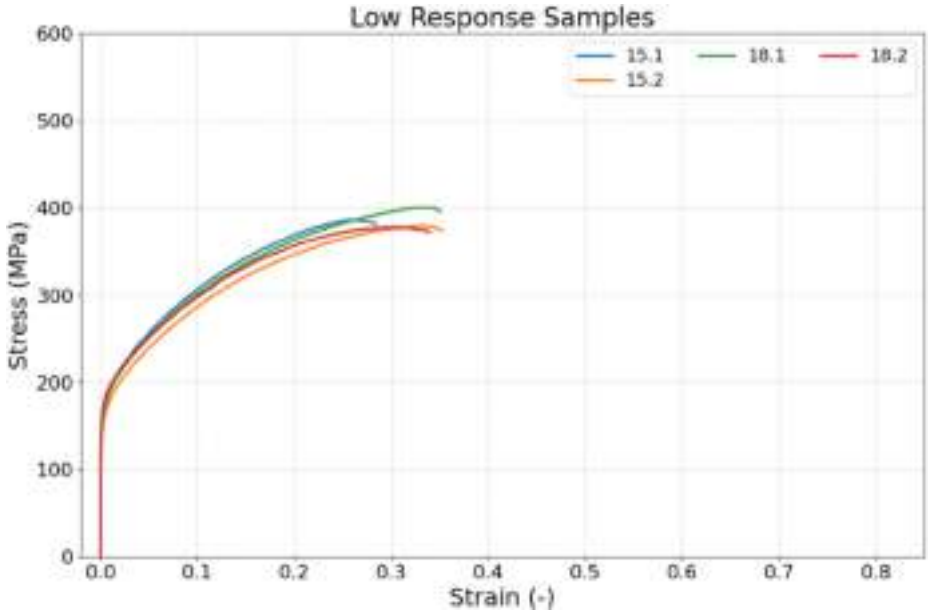

Fig. 4.3. Stress-Strain curves of the low-performing samples, defined in terms of ultimate tensile strength (UTS) and strain at break.

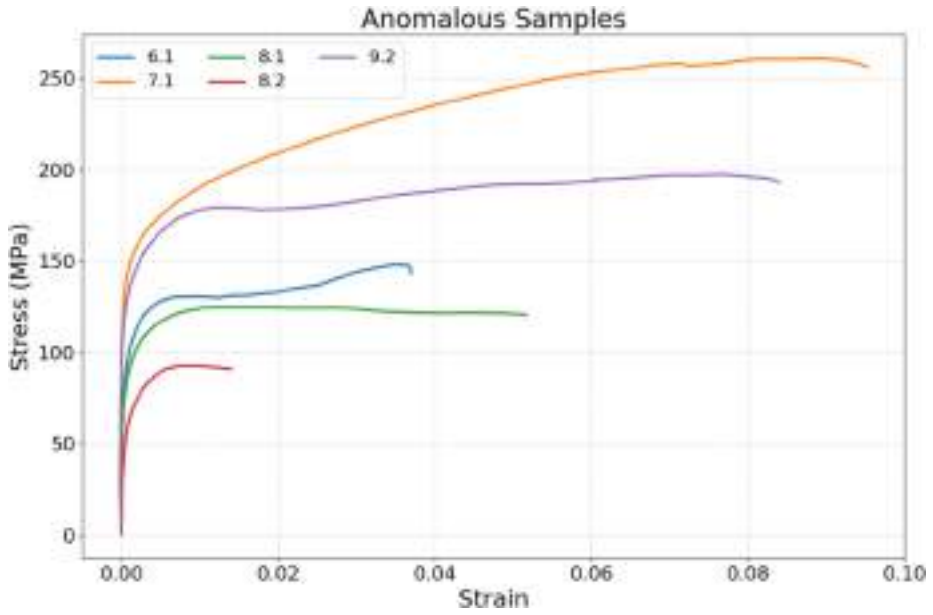

Fig. 4.4. Stress-Strain curves of the anomalous sample, defined in terms of ultimate tensile strength (UTS) and strain at break.

evaluation in the subsequent sections. Violin plots shown in Fig. 4.5. are used to visualise the distribution of each response variable, clearly showing the spread, central tendency, and outliers in the data.

Yield strength values across all samples ranged from 68.6 to 212.3 MPa, with a mean of 156.5 MPa and a standard deviation of 22.4 MPa. Ultimate tensile strength values ranged from 92.9 to 566.0 MPa, with a mean of 426.0 MPa and a standard deviation of 100.1 MPa. Stress at break values ranged from 87.9 to 545.5 MPa, with a mean of 397.4 MPa and a standard deviation of 101.9 MPa. Strain at break values ranged from 0.0370 to 0.8374, with a mean of 0.4613 and a standard deviation of 0.1912. Toughness values ranged from 1.2 MJ/m^3 to 406.4 MJ/m^3, with a mean of 180.9 MJ/m^3 and a standard deviation of 95.6 MJ/m^3. Area error values ranged from 0.0457 mm^2 to 1.3600 mm^2, with a mean of 0.6548 mm^2 and a standard deviation of 0.1172 mm^2.

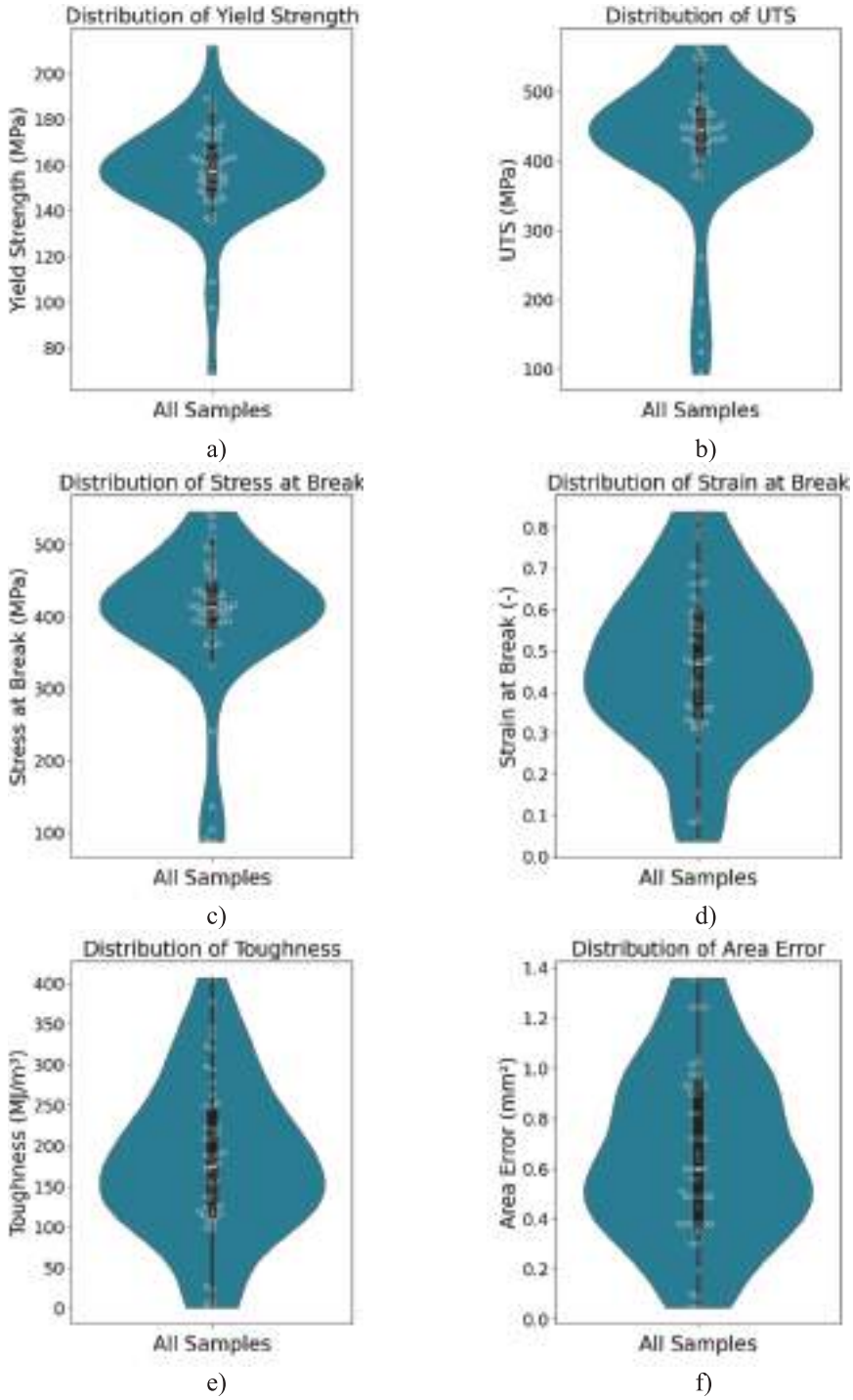

Fig. 4.5. Violin plots showing distribution of data for all six measured responses across all tested samples: a) Yield Strength, b) Ultimate Tensile Strength, c) Stress at Break, d) Strain at Break, e) Toughness, f) Dimensional error.

4.2. Batch influence analysis

The batch factor was included in the statistical analysis to assess its potential influence on the measured responses and occurrence of anomalous samples, as uncontrolled batch-related variation could obscure the true effects of the printing parameters on the material properties. Possible sources of batch variability include differences in filament storage and moisture content, debinding and sintering

conditions, and subtle variations in environmental conditions during fabrication.

During the testing, a total of five anomalous samples were noticed, based on their extremely low values of mechanical responses. Since all five anomalous samples originated from the second batch, this raised concerns that the occurrence of defects might be associated with factors unrelated to the printing parameters. For example, in the anomalous samples, a print speed of 30 mm/s appears in 4 out of 5 cases, which would misleadingly suggest that this speed is strongly associated with poor performance. Similar clustering occurs for other parameter levels. Importantly, all anomalous samples originated from the same batch, indicating that the observed defects are attributable to batch-specific factors, the nature of which is unknown or uncontrollable in this study. Therefore, it would be unrealistic to ascribe these anomalous samples to the printing parameters themselves.

These concerns were validated through Fisher's exact test, which calculated p value of 0.000059, which is much smaller than the common alpha threshold of 0.05. The null hypothesis for Fisher's Exact Test that there is no association between batch and whether an item is defective can therefore be rejected with high confidence, indicating a statistically significant relationship between batch and defect occurrence.

It was concluded that the occurrence of anomalous samples is more likely attributed to factors external to the printing process. Including these anomalous samples in the analysis of printing parameter effects on material responses could introduce bias and compromise the reliability of the results. Therefore, the anomalous samples were excluded from further analysis to ensure an accurate

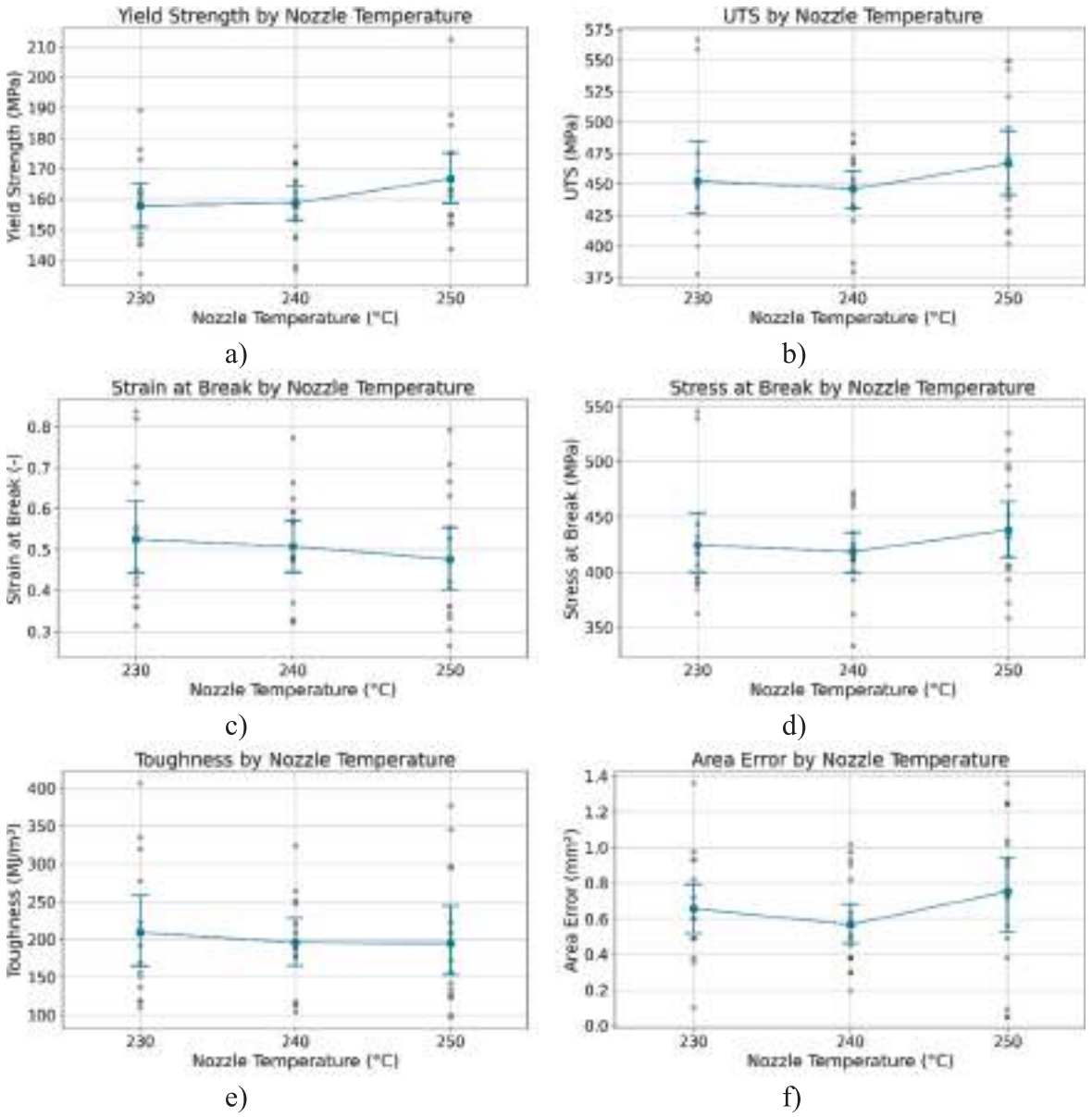

Fig. 4.6. Interval plots showing the mean values and 95% confidence intervals of all measured responses with respect to nozzle temperature.

assessment of the influence of printing parameters on material properties.

Furthermore, these excluded samples highlight the inherent variability in FFF processes, arising from the mentioned batch factors and the repeatability of the printing process. While absolute mechanical values may vary slightly between batches, the observed trends in the influence of printing parameters and porosity on failure mechanisms are expected to remain representative. Careful control of material handling and process conditions is therefore recommended to improve reproducibility in future studies.

4.3. ANOVA analysis effects of printing parameters

In this study, the ANOVA analyses were limited to the main effects of individual printing parameters. Due to the limited number of experimental runs, interactions between parameters were not tested. Therefore, the reported trends reflect only the isolated influence of each parameter, and potential interaction effects remain to be investigated in future work.

Given the conclusions drawn from the batch influence analysis, 45 samples were analysed using ANOVA's general linear model to determine whether some parameters have significant effects on the mechanical response and dimensional accuracy. Out of all the printing parameters, bed temperature showed a significant effect on yield strength, UTS and stress at break, while layer thickness showed a significant effect on dimensional accuracy. To ensure the validity of the analysis, residual plots were examined for all General

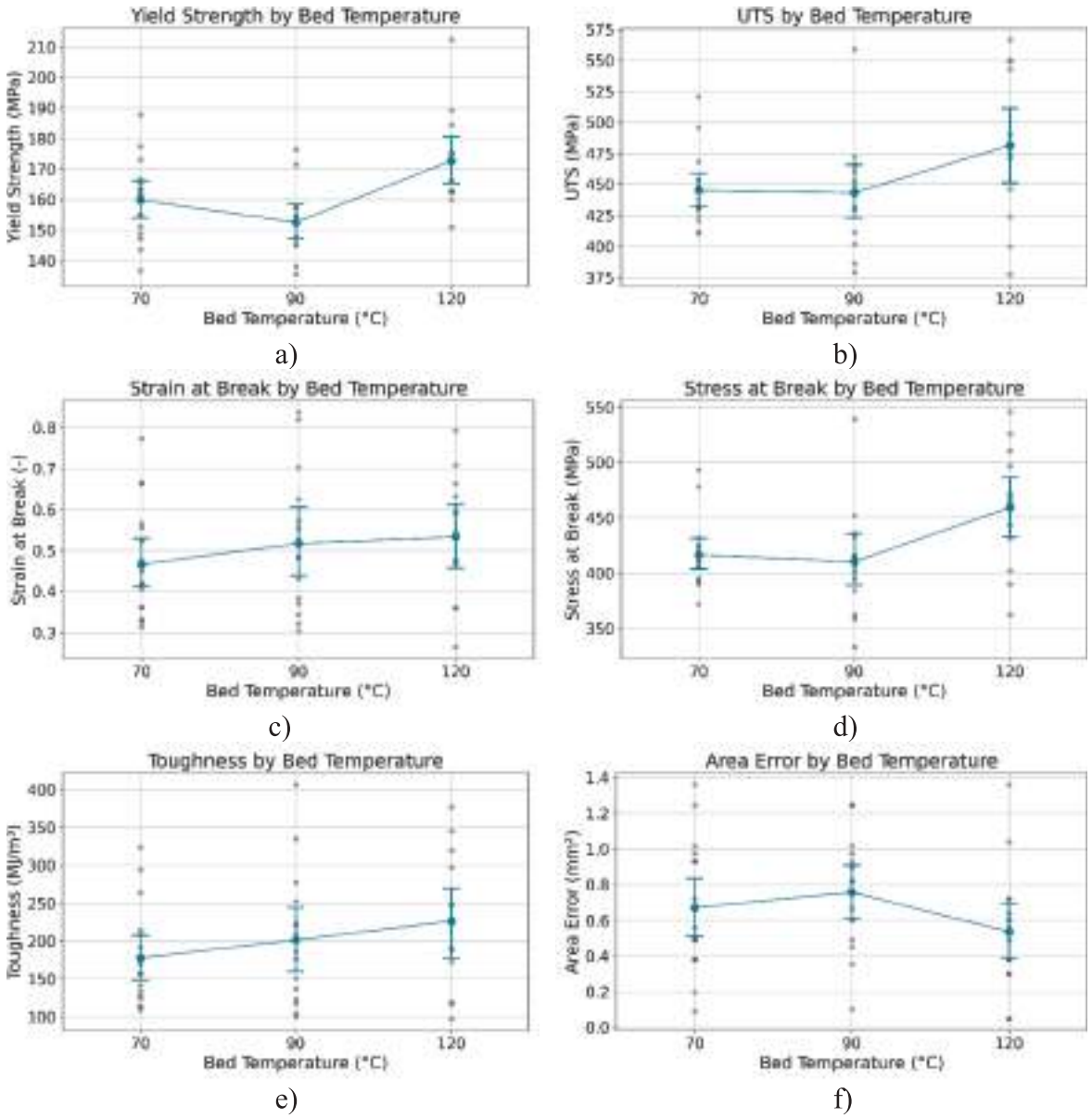

Fig. 4.7. Interval plots showing the mean values and 95% confidence intervals of all measured responses with respect to bed temperature.

Linear Models (GLMs) where factors showed statistically significant effects.

The residuals appear randomly scattered around zero with constant spread, suggesting the model adequately captured the main structure in the data. The normal probability plot shows the residuals are approximately normal, with no major deviations or outliers. The residual histogram is roughly symmetric and bell-shaped, supporting the assumption of normality. The residuals do not show any apparent trend over time, suggesting the process was stable during data collection.

Although the ANOVA analysis did not reveal any statistically significant effects of nozzle temperature on the responses, the interval plots suggest that a nozzle temperature of 250 °C tends to produce slightly higher mean values for yield strength, ultimate tensile strength, and stress at break, while 230 °C appears more favourable for toughness and strain at break and 240 °C for dimensional accuracy. However, the differences in mean values are minimal and may fall within the range of experimental variability or measurement uncertainty (see Fig 4.6).

Bed temperature had a statistically significant effect on yield strength (p = 0.002), with 120 °C producing the highest values. Cohen's *d* was calculated to be 1.5, indicating a high level of practical significance. The ultimate tensile strength was also significantly affected by bed temperature ($p = 0.032$), with 120 °C resulting in the highest values. A Cohen's *d* of 0.8 suggests a substantial and meaningful effect. Stress at break also showed a significant dependence on bed temperature ($p = 0.011$). Maximum values were observed at 120 °C, with a large effect size (Cohen's d = 1.02), indicating substantial practical significance. Outside the significant

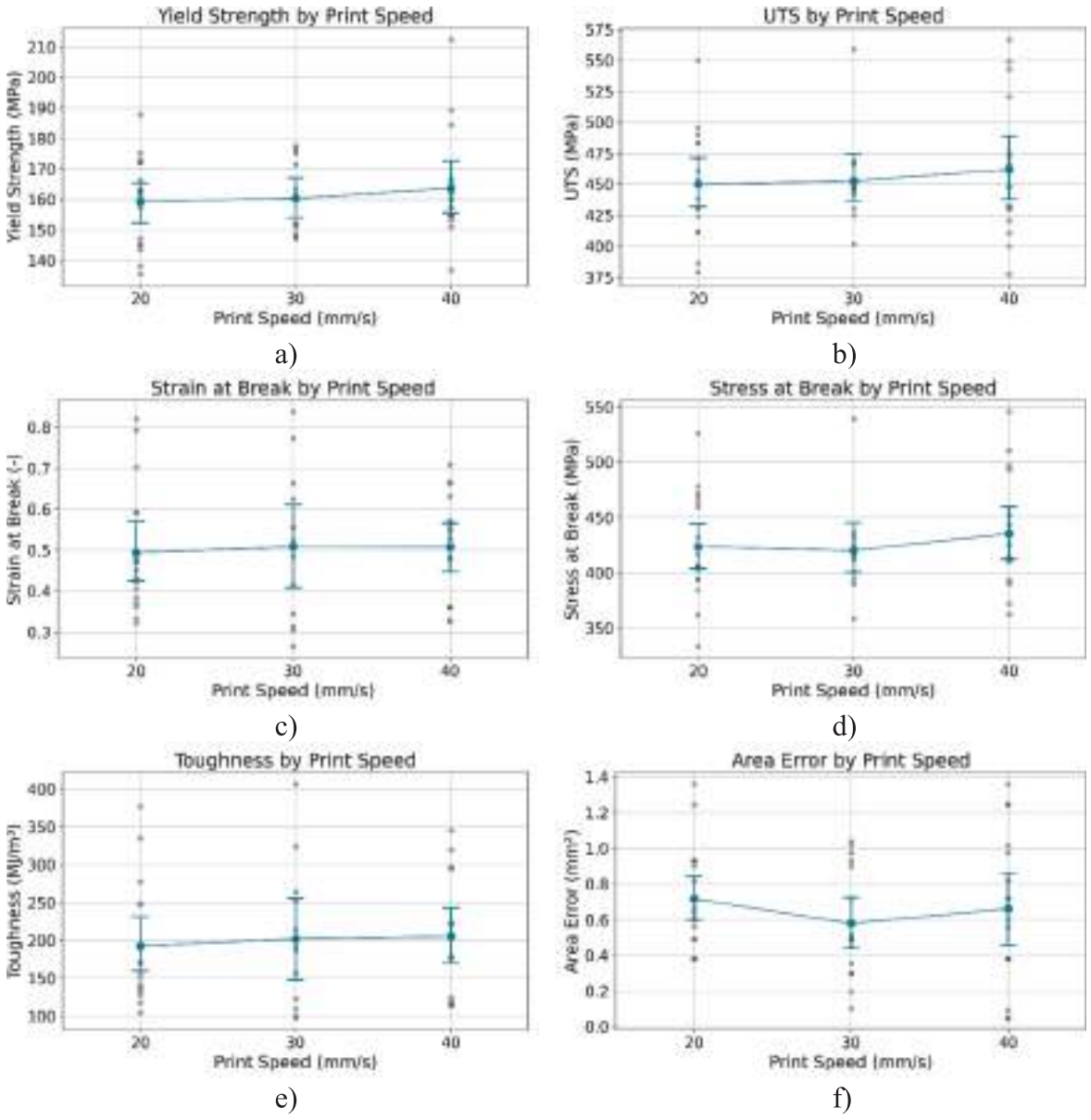

Fig. 4.8. Interval plots showing the mean values and 95% confidence intervals of all measured responses with respect to print speed.

effects observed for yield strength, UTS, and stress at break, the highest bed temperature of 120 °C also resulted, on average, in greater strain at break and toughness, as well as lower dimensional error. Overall, 120 °C demonstrated a preference across all responses, reflected by higher mean values (see Fig 4.7).

Print speed showed no statistically significant effects in ANOVA analysis. However, an examination of the mean response values indicates that the highest print speed of 40 mm/s shows a slight advantage in terms of mechanical properties, while the medium print speed of 30 mm/s is associated with lower average dimensional errors (see Fig 4.8).

Layer thickness had a statistically significant influence on dimensional accuracy ($p = 0.001$). The finest results were achieved with the 0.1 mm setting, and the large effect size (Cohen's $d = 4.75$) highlights its strong practical impact. The coefficient of –0.15 for the 0.1 mm layer thickness indicates that it improved dimensional accuracy by 0.15 mm^2 compared to the reference setting (0.15 mm), since lower values of area error represent better dimensional accuracy. In addition to its significant impact on dimensional accuracy, a thinner layer thickness of 0.1 mm consistently showed higher average values for all the measured responses (see Fig 4.9).

Infill pattern did not show statistically significant effects shown through the ANOVA analysis. However, an examination of the mean response values indicates that the lines pattern showed more optimal mechanical and dimensional response on average (see Fig 4.10).

Similarly, while infill percentage did not show statistically significant effects in the ANOVA analysis, the interval plots reveal that

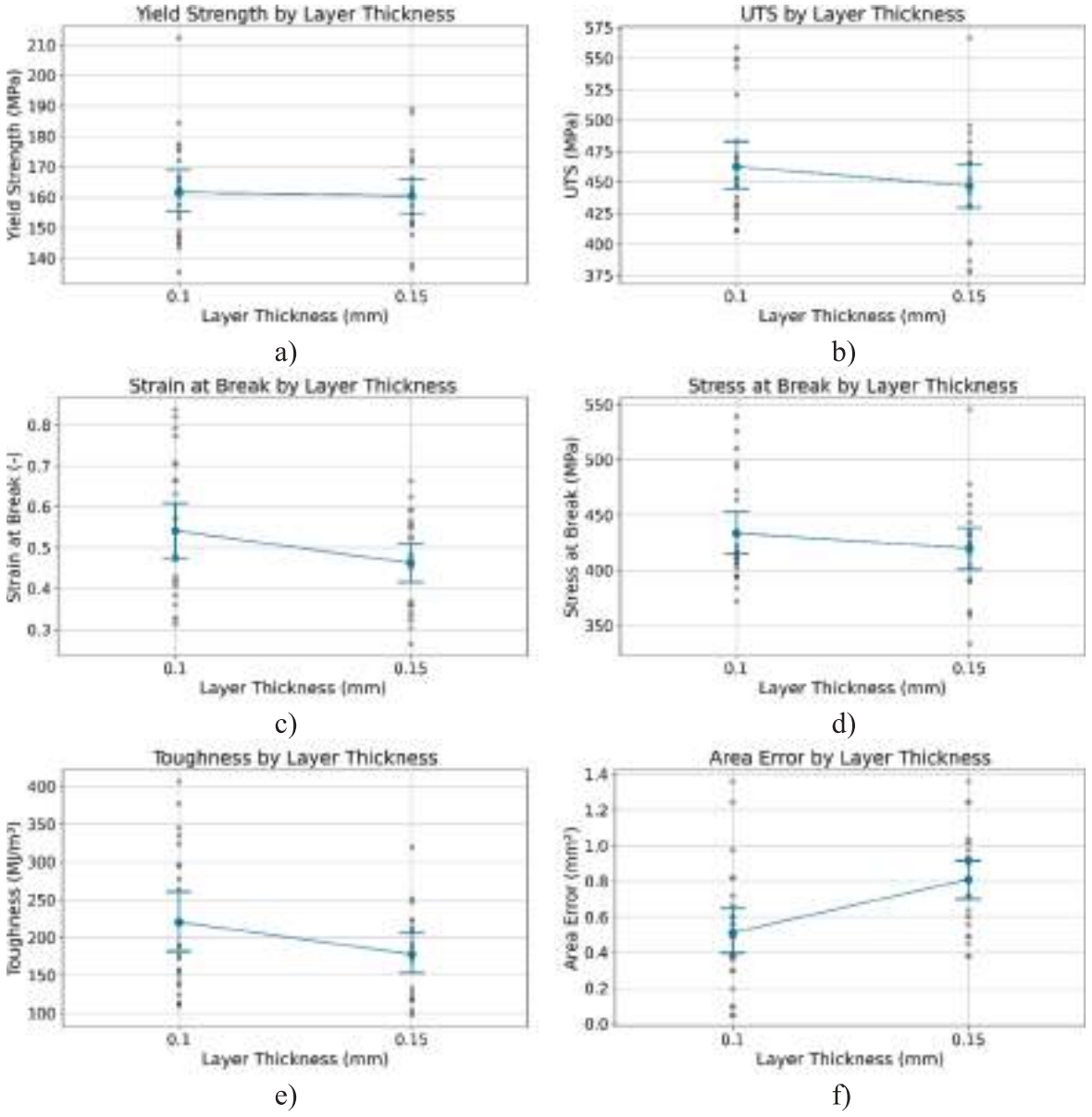

Fig. 4.9. Interval plots showing the mean values and 95% confidence intervals of all measured responses with respect to layer thickness.

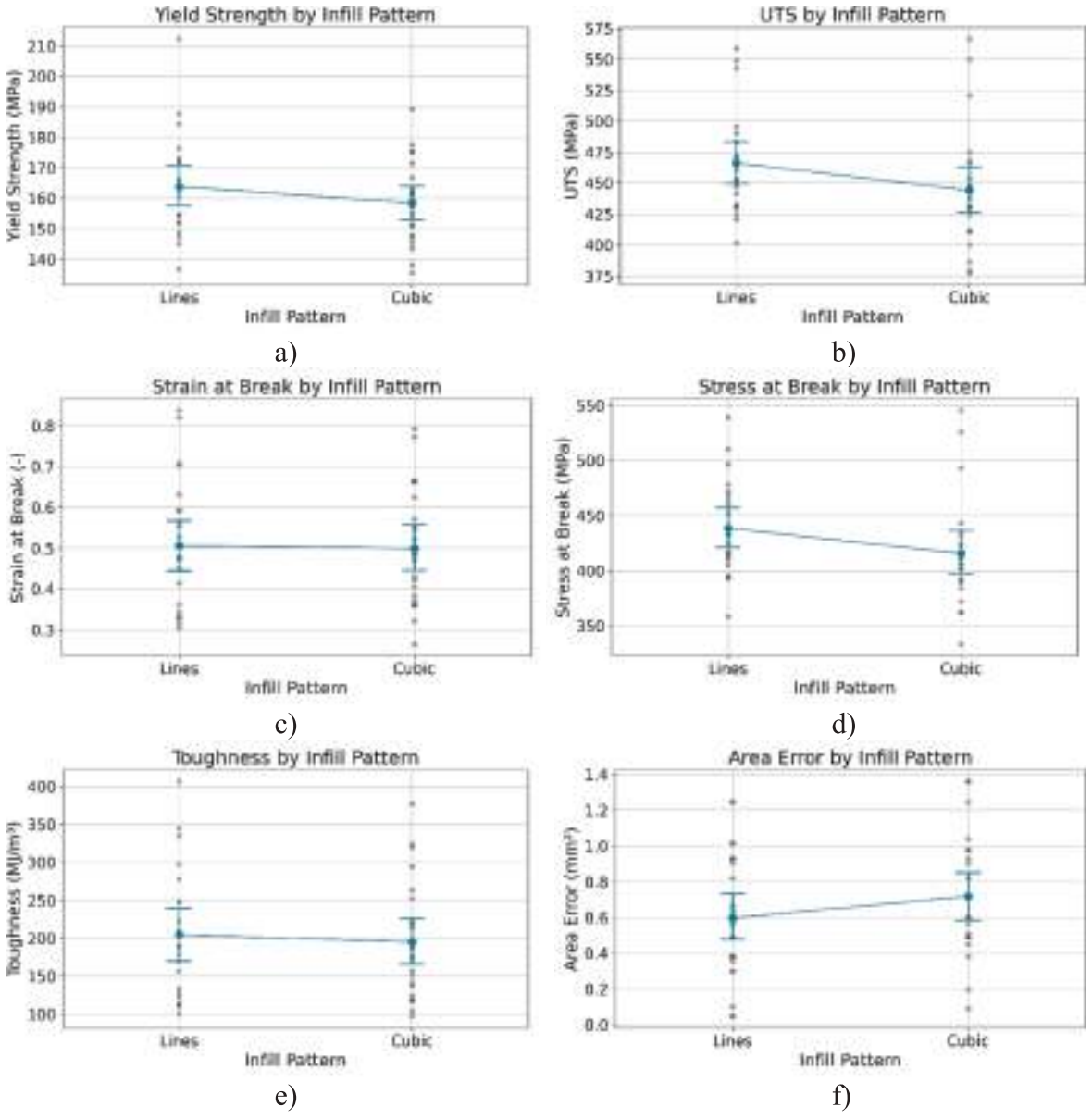

Fig. 4.10. Interval plots showing the mean values and 95% confidence intervals of all measured responses with respect to the infill pattern.

the lower infill level of 100 % generally produced higher average mechanical responses and lower dimensional errors compared to the 105 % infill (see Fig 4.11).

4.4. Robustness analysis

ANOVA analysis of the printing parameters highlighted bed temperature and layer thickness as the most influential factors. Additional trends suggesting more optimal responses were observable in the interval plots, even when not statistically significant. However, to provide a more comprehensive evaluation, the analysis was extended to identify specific parameter levels that not only yield higher mean mechanical properties and reduced dimensional errors but also offer improved consistency, contributing to better process predictability. This was achieved by applying Taguchi's signal-to-noise (S/N) ratio method.

Normalised S/N ratio values were transformed into grey relational coefficients, and a grey relational grade (GRG) was then used to determine which parameter level results in higher S/N ratios across all responses (Fig. 4.12).

Robustness analysis approach through S/N ratios and grey relational analysis shows that the following parameters produce more consistent and better mechanical and dimensional responses: nozzle temperature of 250 °C, bed temperature of 120 °C, print speed of 40 mm/s, layer thickness of 0.1 mm, lines infill pattern and a 100 % infill percentage.

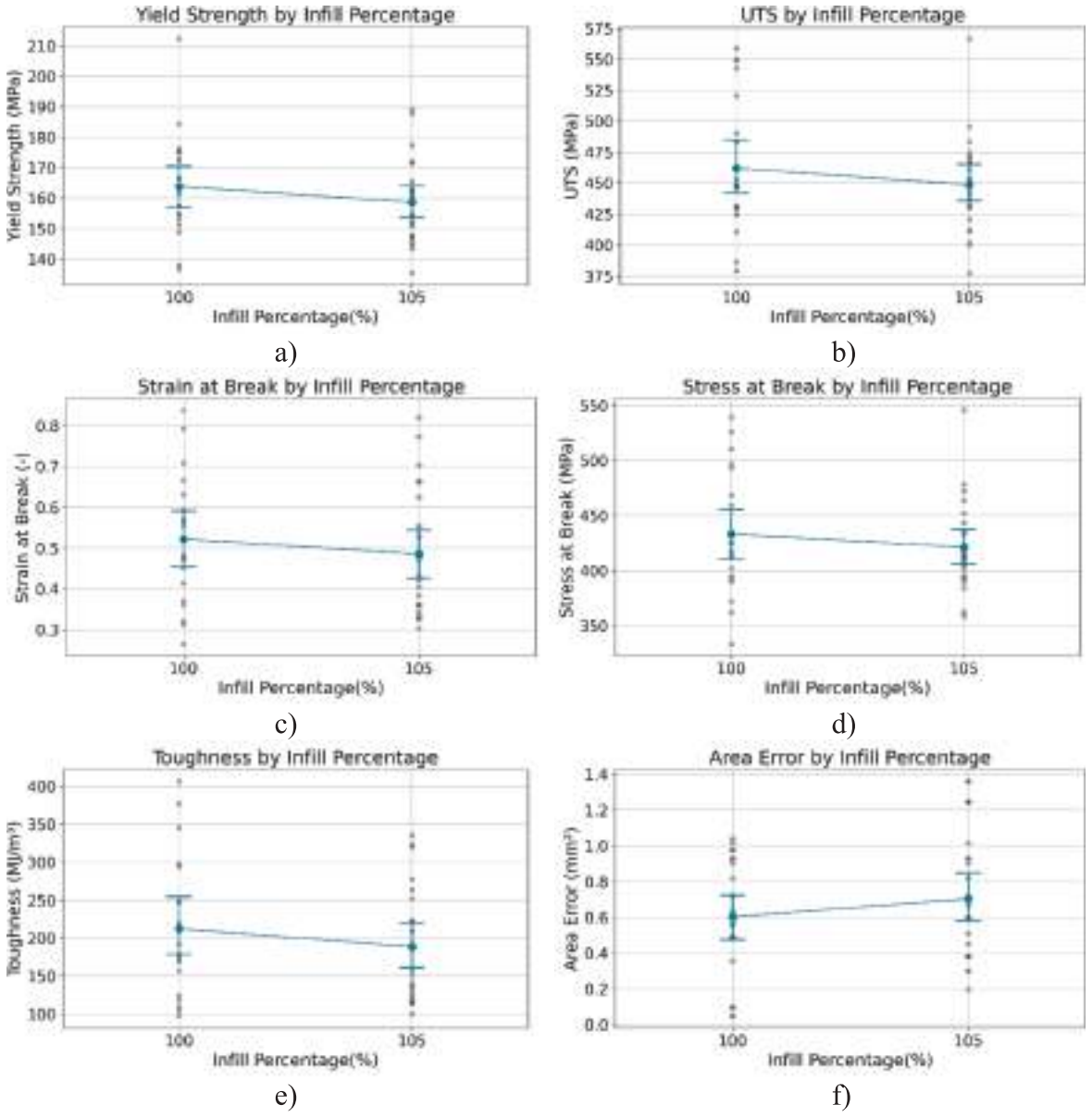

Fig. 4.11. Interval plots showing the mean values and 95% confidence intervals of all measured responses with respect to infill percentage.

While ANOVA identified bed temperature as a statistically significant factor for yield strength, UTS, and stress at break, and layer thickness for dimensional accuracy, the influences of other parameters (nozzle temperature, print speed, infill pattern, and infill percentage) did not reach statistical significance. Observed trends in GRG and S/N ratios are reported to indicate potential effects and provide guidance for parameter selection, but these should be interpreted as suggestive rather than conclusive.

4.5. Hardness measurements

Hardness measurements were performed to evaluate the mechanical response of the sintered material using the Rockwell B hardness test (HRB). However, the presence of pores within a material diminishes its resistance to indentation, as these voids act as weak points that deform or collapse when subjected to load.

Due to the high porosity of the samples, many measurements yielded values that were either below the measurable range of the applied hardness scale or otherwise unreliable, limiting the representativeness of the results. For this reason, the hardness measurements were excluded from the parameter evaluation analysis.

The HRB measurements of the material exhibited a mean value of 35.46 with a standard deviation of 19.89, reflecting the variability across the tested samples. Most measurements ranged between 40 and 50 HRB, while the maximum value recorded was 69.70.

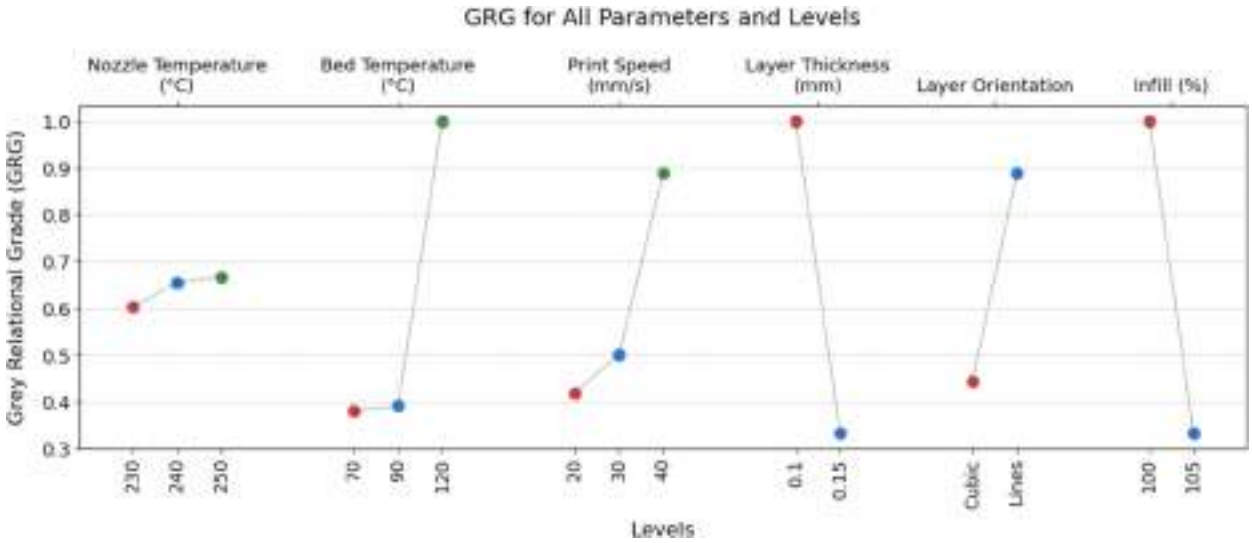

Fig. 4.12. Grey relational grades for all levels of the considered printing parameters.

Certain measurements yielded a HRB value of 0, indicating that the material was too porous to provide reliable hardness values. This variability may indicate microstructural inhomogeneities, such as localised porosity or inclusions, although hardness measurements alone cannot provide a quantitative assessment of porosity. The distribution of hardness measurements is shown in Fig. 4.13.

The measured average hardness is lower than typical values reported for 316L stainless steel, which can be attributed primarily to the presence of porosity. Although hardness was not analysed in relation to the printing parameters, previous studies have demonstrated a clear correlation between hardness and defect density [41], supporting the interpretation that porosity is the main contributor to the reduced hardness observed in our samples.

4.6. Fractography analysis

To interpret the mechanical responses observed during tensile testing and explain the variations between parameter configurations, a detailed fractographic analysis was conducted on selected specimens to identify failure mechanisms and assess the influence of internal defects or manufacturing irregularities. Fractography was performed using SEM to analyse the material porosity, potential defects that might have had effect on material behaviour and the overall nature of the microstructure of FFF-manufactured stainless steel. A sample 7.2. was chosen for the analysis as a representative sample, as it demonstrated properties closely aligned with the overall average for all measured responses.

At first glance (see Fig. 4.14), delamination can be seen at the top part of the sample, where the top layer separated during the tensile test. Furthermore, significantly high porosity can be seen across the entire analysed fracture area, with a layered-based

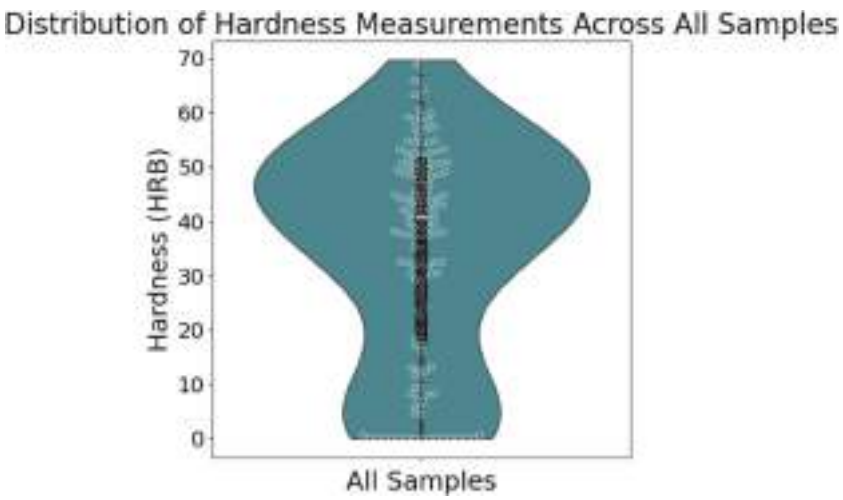

Fig. 4.13. Distribution of Hardness HRB measurements.

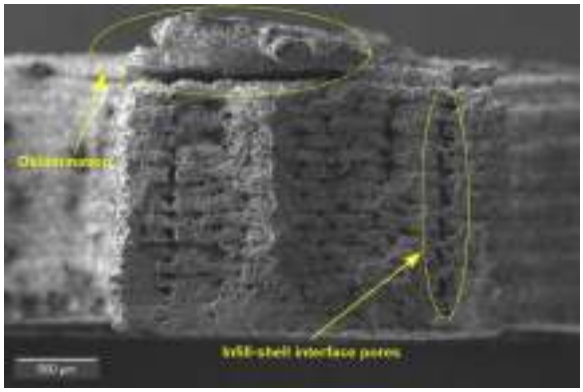

Fig. 4.14. Fracture surface revealing high porosity and the characteristic layered structure resulting from the additive manufacturing process.

microstructure that is noticeable. Interlayer pores appear to dominate, consistent with the layer-by-layer nature of the manufacturing process.

Large pores can be seen between the infill and outer layers, connected in a big vertical pore across the entire sample. This can be attributed to the different print pattern between infill, the outer layers and the nozzle path not being able to completely fill and cover that transition.

SEM scan based on circular backscatter detector (CBS) is shown in Fig. 4.15. highlights the porosity on the material fracture surface. In addition to the large interlayer pores, smaller pores are also visible throughout the fracture surface, likely resulting from incomplete sintering and residual binder removal during the manufacturing process.

Characterised by smooth surface and edges, the macro pores inside the material structure can be observed (Fig. 4.16). These pores appear smooth, rounded and untouched, which suggests these parts were not directly involved in the fracture but were just pores/defects that were located near the fracture. In contrast, regions directly affected by fracture typically show rough surfaces, highlighting the distinction between pre-existing defects and fracture-generated features.

These pores account for a significant portion of the overall material porosity observed on the fracture surface and are predominantly located between layers. Their presence highlights the high porosity resulting from the layer-by-layer nature of the manufacturing process and possible inconsistencies during the printing process. Interlayer macro pores are randomly distributed throughout the material and vary in both size and shape.

Surrounding the smooth macropore, a mixture of dimples of various sizes is observed, characteristic of ductile fracture, suggesting non-uniform stress distribution within the material.

The presence of dimples on the fracture surface represents the part of the material that underwent ductile fracture. Observed dimples can be described as deep and narrow, which indicates the high ductility of the material. High ductility of the material can also be observed trough surface steps visible on dimple walls. Dimple size is dependent on the particle size. A mixture of dimple sizes is observable which is normal for metal materials since they have a combination of large and small particles.

While the overall fracture surface is dominated by equiaxial dimples, characteristic of uniform load distribution during tensile testing, certain regions exhibit so-called shear dimples (see Fig 4.17). These types of dimples have an oval shape and are usually formed on the lateral fracture surfaces. The appearance of these types of dimples suggests that a local multiaxial stress state arose during the fracturing process, probably due to stress concentrations between layers and anisotropy introduced by the layered structure.

This coexistence of smooth, undisturbed pores and fracture-related features like sharp edges and dimples can be seen throughout

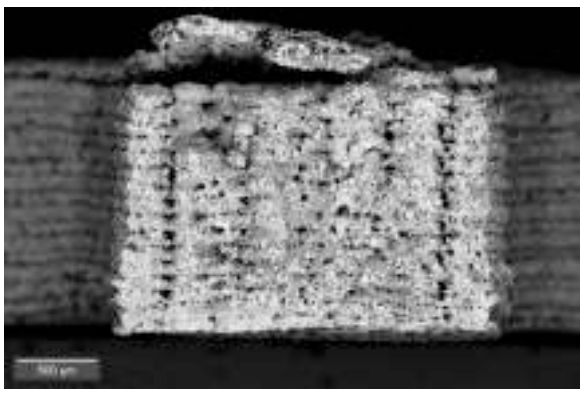

Fig. 4.15. Fracture surface enhanced using CBS showing high porosity fracture surface.

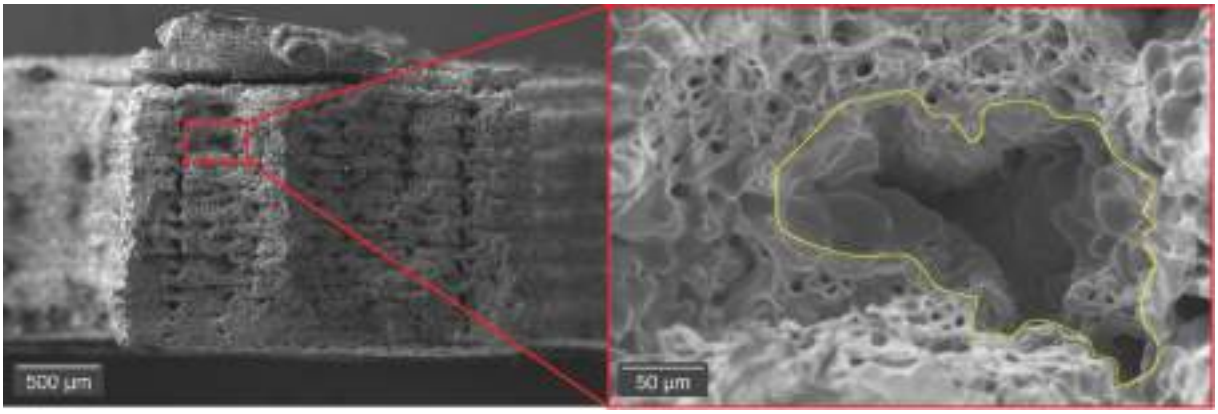

Fig. 4.16. Smooth untouched pore (highlighted in yellow) surrounded by dimples showing ductile fracture.

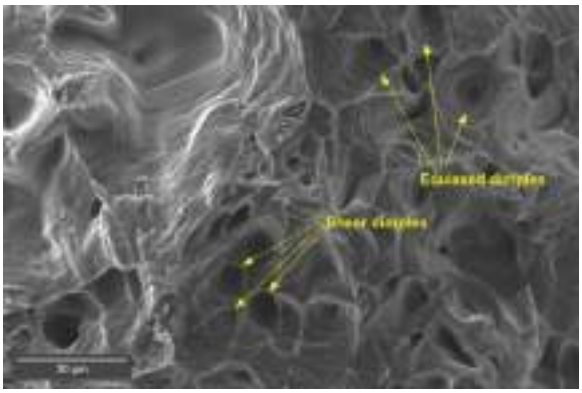

Fig. 4.17. Fracture surface showing a mixture of equiaxed and shear dimples, indicating a non-uniform stress distribution.

the material (Fig. 4.18). This implies that stress was not uniformly distributed across the sample, with certain regions, especially around inter-layer pores, experiencing little to no load transfer.

After examining the average-performing samples, attention was turned to the highest-performing specimen, 9.1, which featured a line infill pattern. This analysis aims to investigate the porosity in high-performing samples and to assess whether the observed mechanical properties correlate directly with porosity. Fig. 4.19 shows the fracture surface of sample 9.1, highlighting a reduced porosity compared to the average-performing sample 7.2.

Sample 9.1., while still highly porous, showed a reduced number of smooth untouched pores, suggesting more uniform strain distribution (Fig. 4.20.).

To further investigate the influence of infill patterns on mechanical performance, specimens with cubic infill were considered. Among these, Sample 2.2, the highest-performing specimen with cubic infill, stood out in terms of overall performance and was analysed in detail (Fig. 4.21). This specimen was selected due to suspicion that the cubic infill pattern may have a higher tendency to create macro-pores due to its geometric arrangement, which can increase the possibility of defects. Fig. 4.21 shows a macro pore near the centre of the sample with a smooth, undisturbed surface, suggesting it existed prior to fracture and indicating a potential tendency of the cubic infill pattern to generate larger defects.

4.7. Strain mapping

Total strain along the loading direction was mapped on high- and average-performing samples to analyse for non-uniform strain distribution, typical of AM-induced microstructural heterogeneity. Results show correlations between the position of macro pores and higher strains.

Strain mapping analysis of a sample 7.2. revealed strain localisation precisely at the position of the macro pore previously identified using SEM analysis. Fig. 4.22 presents the localised strain identified through strain mapping, along with the corresponding macro pore observed in the SEM analysis. At the moment captured in the figure, the nominal strain measured in the sample was approximately 0.4474.

Highest performing cubic infill sample 2.2. was checked for strain localisation due to the macro pore noticed in the SEM analysis. Strain localisation was again observed in the same region where the macro pore was detected through SEM analysis (Fig. 4.23). At

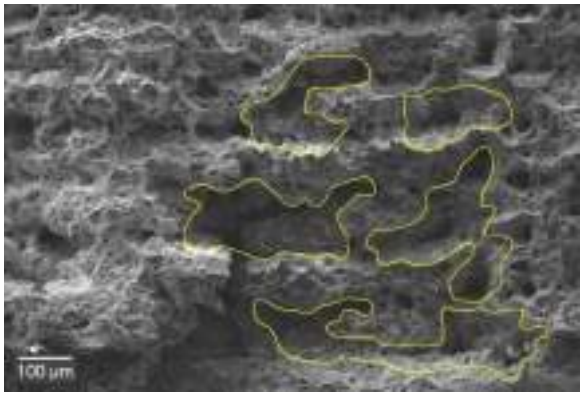

Fig. 4.18. Fracture surface showing a mixture of fracture-related features and smooth untouched regions (highlighted in yellow).

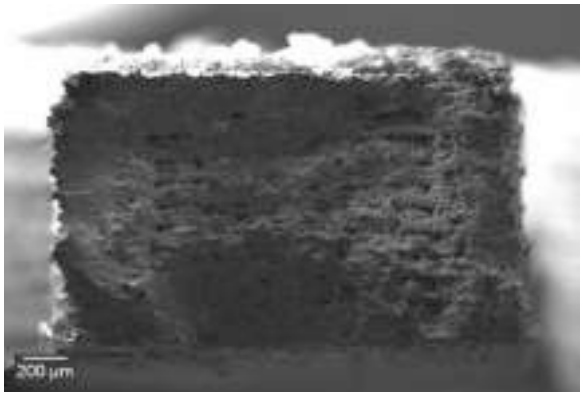

Fig. 4.19. Fracture surface of 9.1 sample showing reduced porosity.

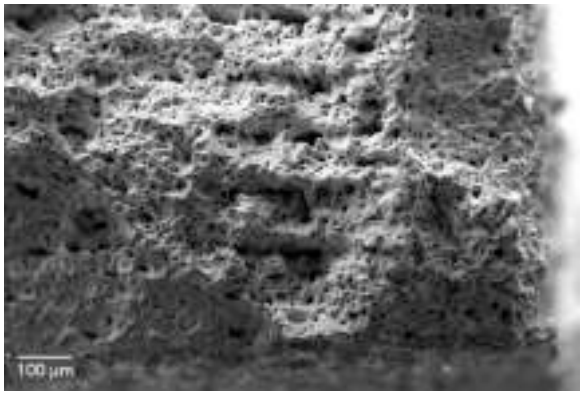

Fig. 4.20. Fracture surface of sample 9.1, indicating fewer smooth, untouched pores.

the stage illustrated in Fig. 4.23, the nominal strain in the sample was approximately 0.6295.

The highest-performing sample 9.1, printed with a lines infill orientation, was also examined to investigate whether strain localisation occurred in high-performing specimens. SEM fractography of sample 9.1. showed reduced porosity overall and a significantly smaller number of macro pores. Furthermore, strain mapping analysis showed uniform strain distribution (Fig. 4.24). At this point in the test, corresponding to the figure, the global strain was approximately 0.7972. This observation indicates the potential to reduce porosity and strain localisation through optimisation of fabrication methods.

Strain mapping results indicate a direct correlation between material defects and localised deformation. By comparing these strain maps with SEM fractography images, a clear relationship between porosity and strain localisation is observed. This comparison highlights how defects such as interlayer pores act as initiation sites for concentrated strain during deformation.

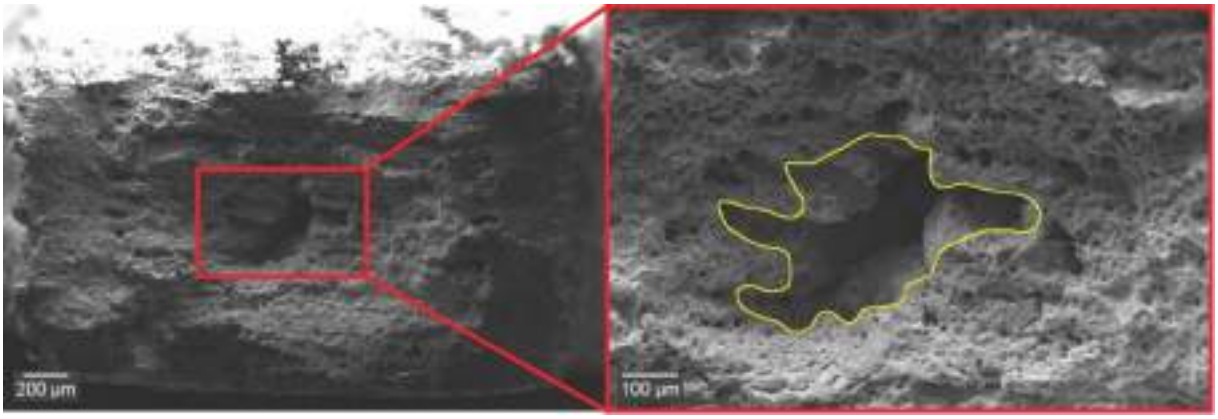

Fig. 4.21. Overall fracture surface and detailed view of a smooth macro-pore (highlighted in yellow) in a cubic-infill sample.

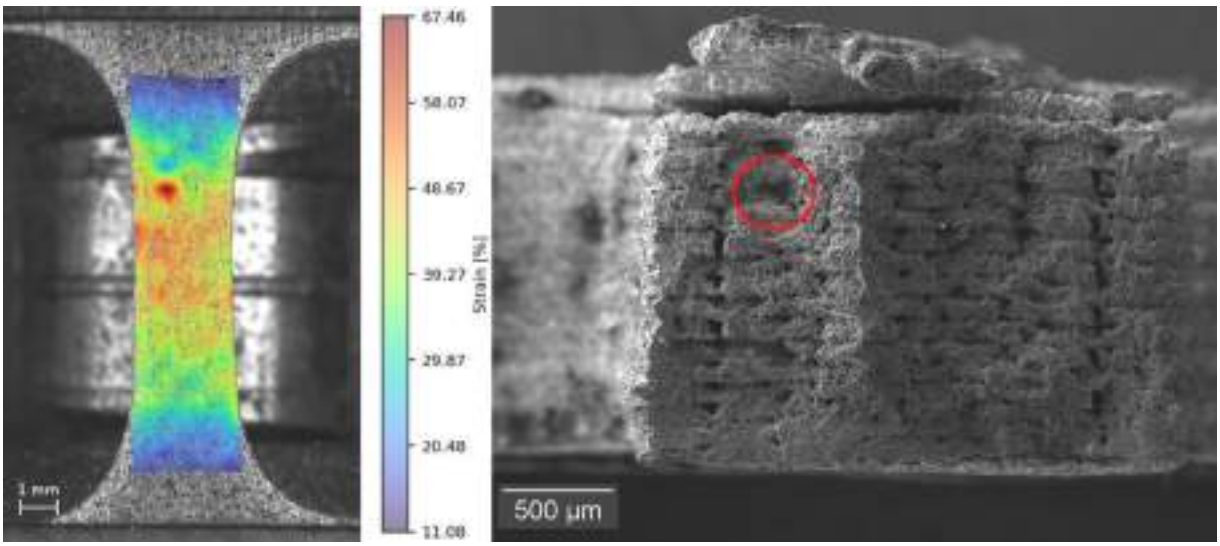

Fig. 4.22. Strain mapping analysis of sample 7.2. showing correlation between macro pore position and localized strains.

4.8. Porosity and defect analysis

While the previous analysis focused on fracture-related features, the subsequent porosity assessment allowed identification and characterization of pores present in the material prior to testing, independent of fracture effects. Porosity measurements were performed on cut surfaces from regions of the samples unaffected by tensile testing. This approach provided more detailed imaging, enabling clearer identification of pore shapes and types, and facilitated more systematic classification of defects. Eight samples with average overall mechanical responses were analysed in this study (Fig. 4.25).

The pores identified in the samples were classified into three main types: printing-associated pores, gas entrapment pores, and sintering residual pores.

Printing-associated pores or extrusion defects are observed as large pores of irregular shape caused by defects in the printing stage of the manufacturing process, mostly due to insufficient bonding between adjacent layers and inconsistencies during extrusion of the filament (Fig 4.26). They usually form between adjacent layers and tend to align with the printing direction [29]. Notably, these printing-associated pores correspond to the large, irregular, smooth pores observed in the fracture surfaces during the earlier fractography analysis. These pores are generally too large to close during the sintering stage and, in many cases, account for a significant portion of the total porosity [30]. Here, we can differentiate between surface-connected pores and internal pores (Fig. 4.26). Their area size ranges from around ~250 μm^2 for small printing irregularities up to ~60000 μm^2 corresponding to significant discontinuities in the printing process. Pores smaller than these dimensions are attributed to the debinding and sintering stages of the process.

Gas entrapment pores are caused by leftover binder-decomposition gases and trapped binder. These pores appear and evolve during the debinding and sintering part of the process. During the binder removal decomposition generates gaseous products. If the binder network has insufficient porosity channels, gases can get trapped. The trapped gas generates internal pressure, enlarging the pores of

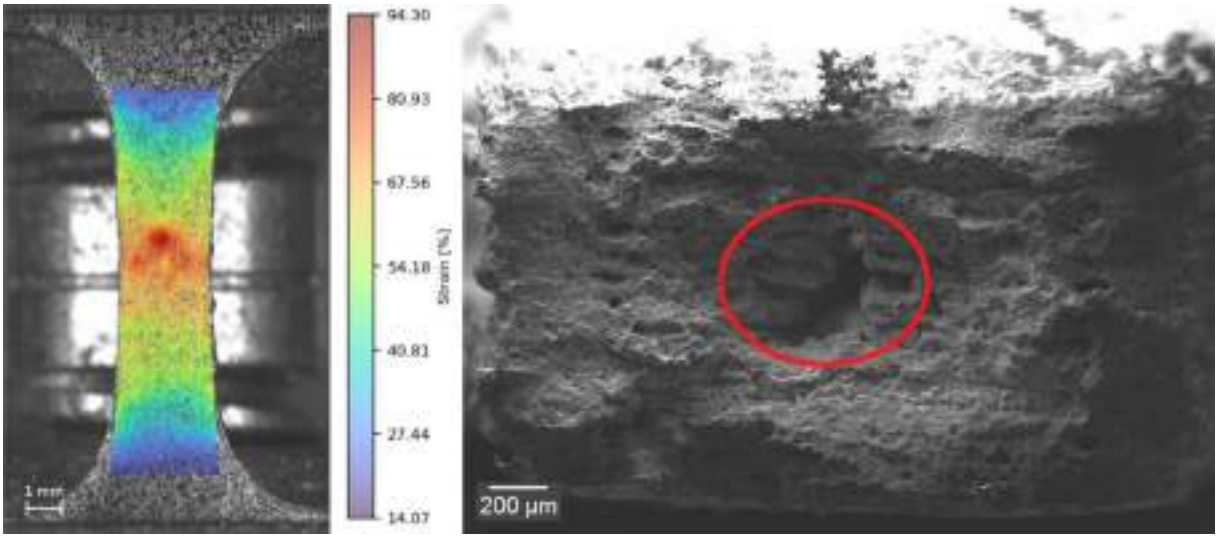

Fig. 4.23. Strain mapping analysis of sample 2.2. showing correlation between macro pore position and localized strains.

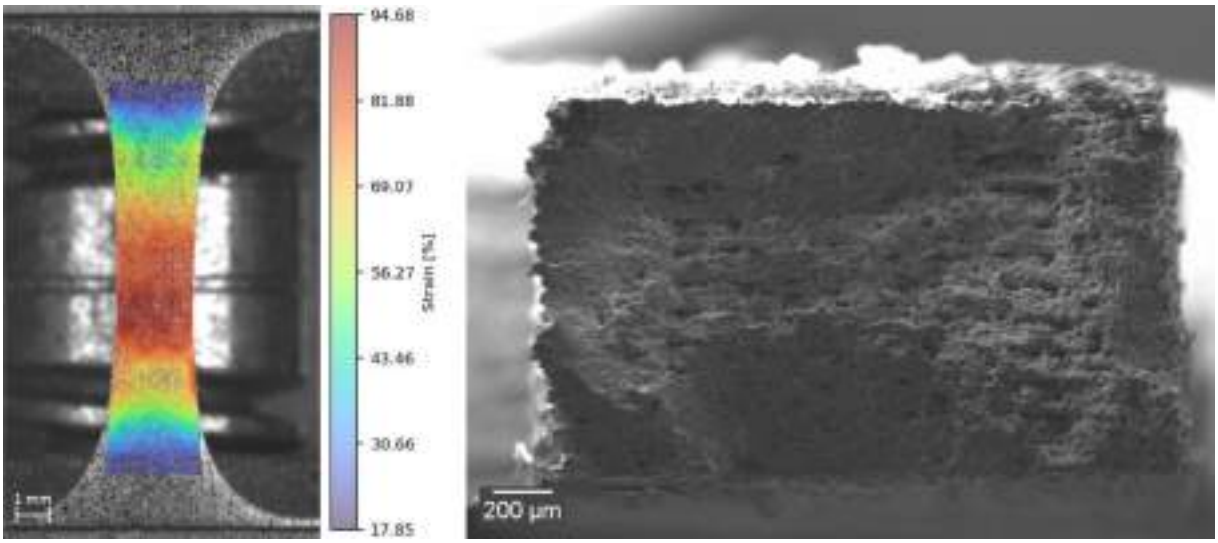

Fig. 4.24. Strain mapping and SEM fractography of sample 9.1. demonstrating improved strain uniformity and reduced porosity.

spherical shape with smooth walls. [42,43] These gas-filled pores often remain after sintering because the gas cannot escape through the surrounding material. The size of these pores is measured at approximately 30–50 μm^2, however in some cases the area of these pores reaches up to 150 μm^2. Fig. 4.27c shows the largest gas entrapped pore observed (150 μm^2), located near the large printing-associated pore, among several smaller gas-entrapped pores in the surrounding area.

During the sintering stage, metal particles fuse together, reducing the pores between them. In the green parts and the initial stage of sintering, pores between the metal particles are usually irregular, elongated or branched. Ideally, in the final stages of sintering, these pores tend to become spherical due to minimisation of surface energy.[31,44–46] However, if the material is constrained, or the pores are trapped in rigid regions, they may remain irregular. [32,47].

Another potential cause of irregular shape sintering residual pores in FFF-manufactured parts is non-uniform green part density and consequently anisotropic shrinkage or densification, which originates from the intrinsic layered structure, variations in local density and the presence of unevenly distributed pathways from binder removal. This leads to the creation of voids in regions where particles are less densely packed. Due to this anisotropic shrinkage and heterogeneous density, pores in FFF components may remain irregular rather than becoming spherical, as typically observed in conventionally sintered metals. [31–34,48,49] The size of sintering residual pores is measured up to 250 μm^2.

Fig. 4.27a and 4.27b shows irregular sintering pores surrounded by spherical gas entrapment pores. While some of the observed spherical pores may correspond to regular sintering pores as well as gas entrapment pores due to their overlapping size and

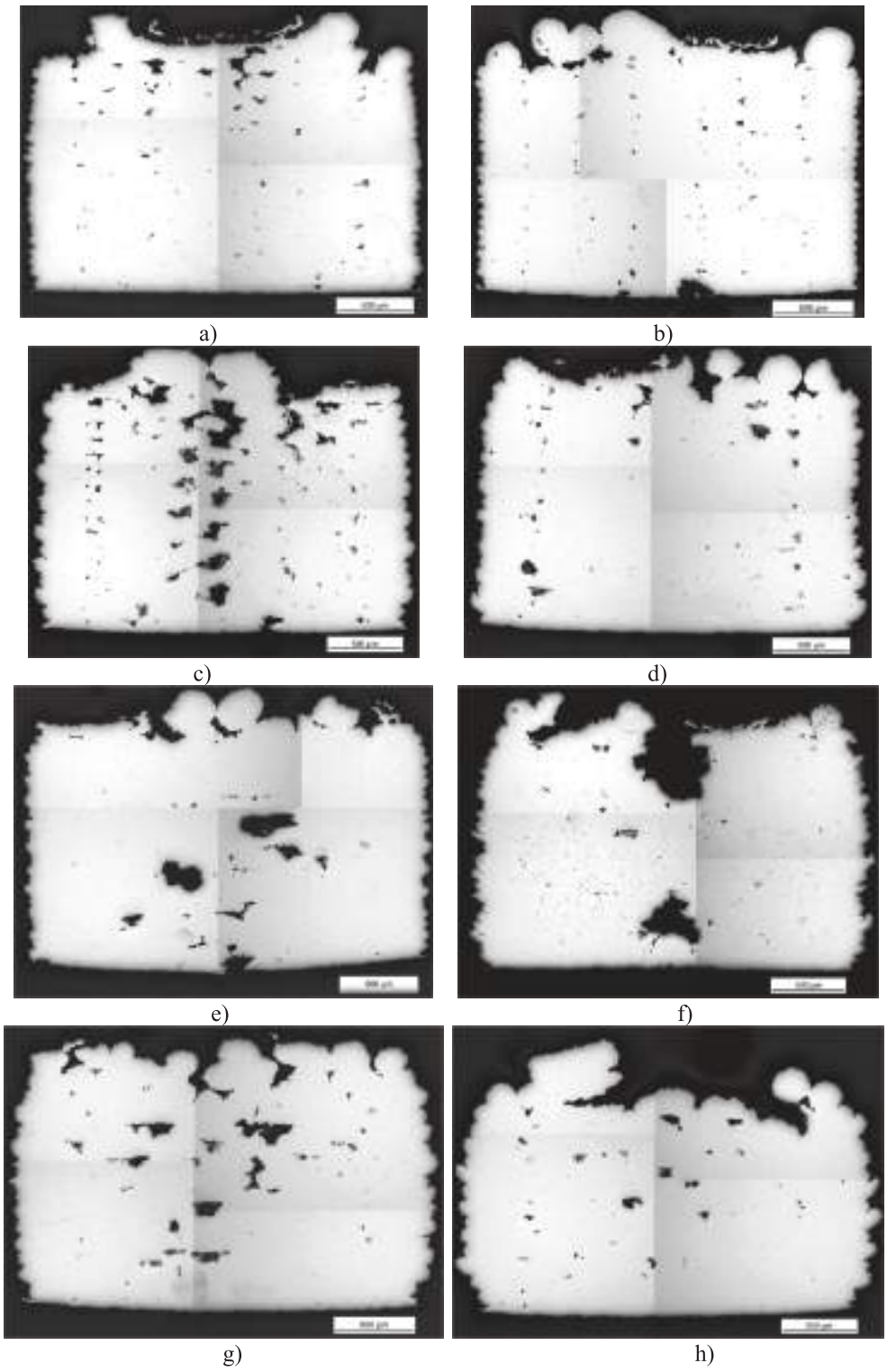

Fig. 4.25. Porosity Analysis of the following samples: a) 10.1, b) 16.2, c) 11.1, d) 4.1, e) 21.1, f) 3.2, g) 23.1, h) 25.1.

morphology, the two types can generally be distinguished based on shape and surface texture. Gas-entrapped pores are typically smooth-walled and nearly spherical, whereas residual sintering pores can appear in either irregular shape or only partially rounded because they originate from incomplete particle rearrangement and neck growth rather than trapped gas bubbles.

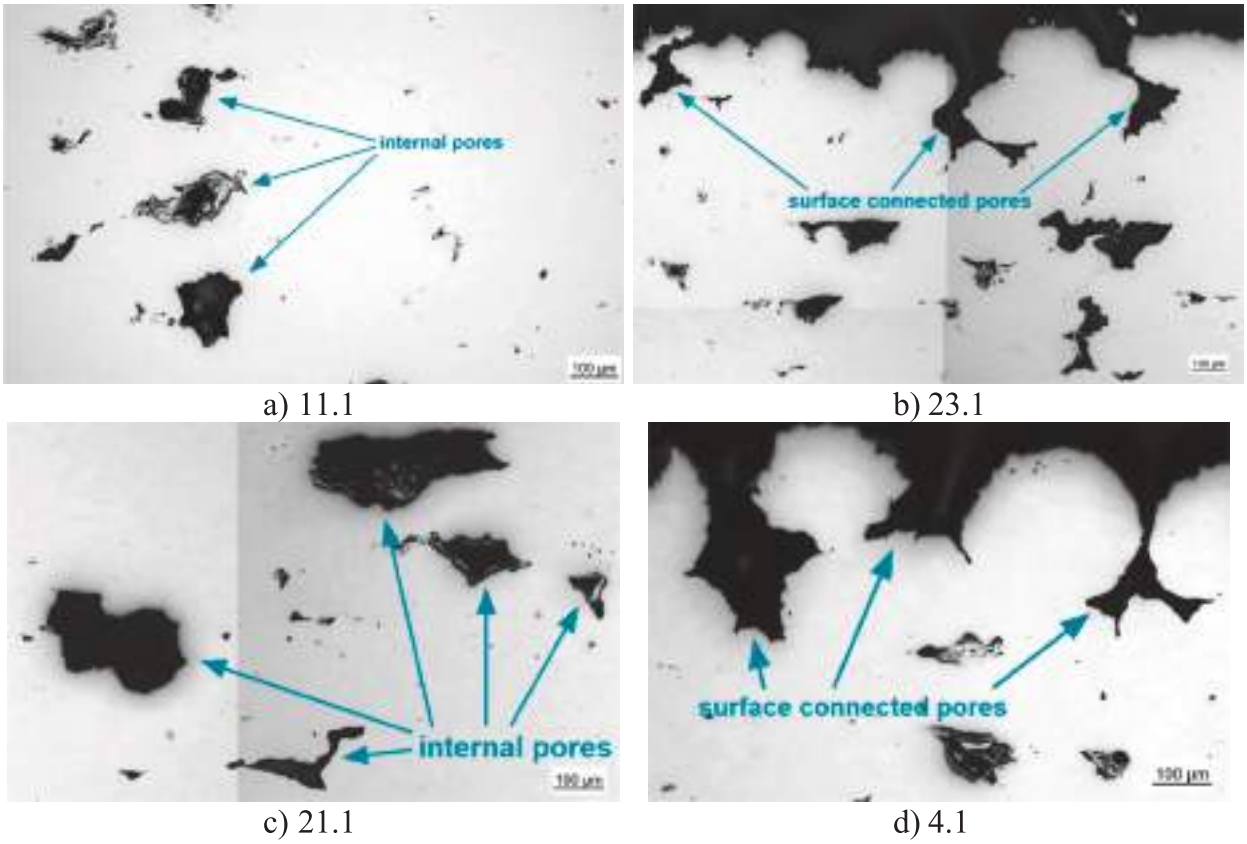

Fig. 4.26. Internal and surface connected printing-associated pores.

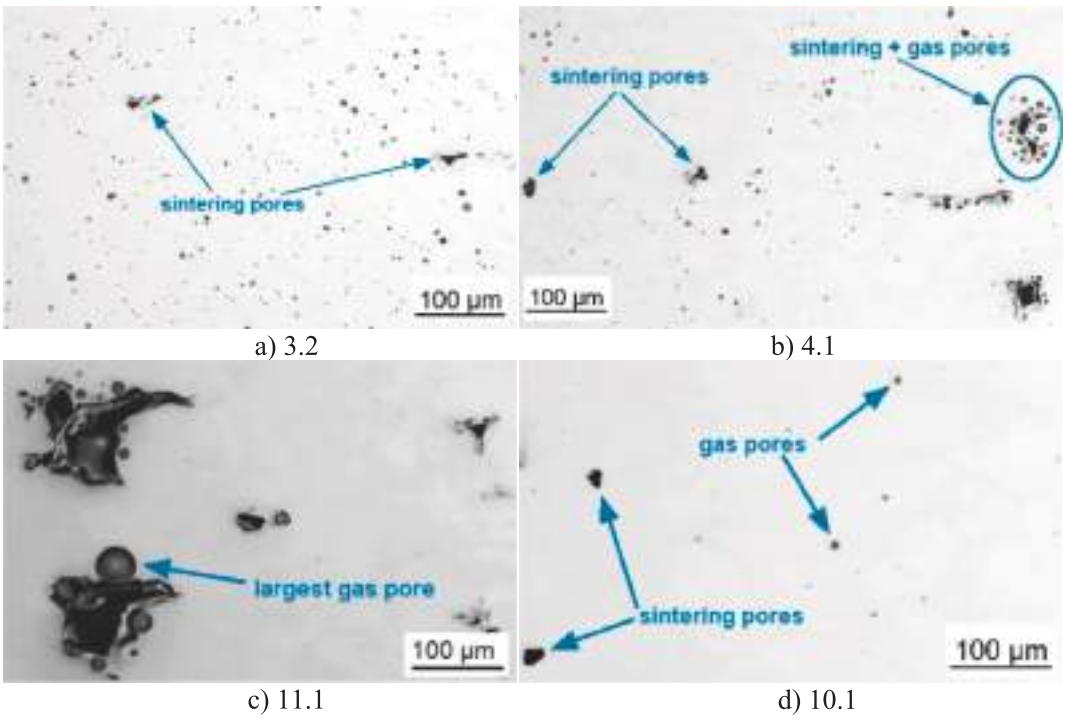

Fig. 4.27. Examples of gas entrapped and sintering residual pores.

In this study, porosity quantification focused on closed (internal) pores, excluding surface-connected pores. Closed pores are fully enclosed within the material and can be precisely measured in 2D cross-sections, whereas surface-connected pores have borders that are not clearly defined at the sample surface, making it difficult to determine their true area in a reproducible manner. By limiting the analysis to closed pores, the measured porosity reflects well-defined voids within the bulk material, enabling consistent comparison of pore size, shape, and distribution across different samples.

Closed porosity analysis was conducted on the cut cross-sections, revealing values ranging from 0.87 % to 5.42 % (Table 4.1). Porosity was calculated as the total pore area divided by the true measured cross-sectional area of each sample. Although these measurements do not fully represent the overall sample porosity, they provide a clear indication of its variability. Comparison with cross-section scans shows that porosity is primarily influenced by printing-associated pores, with samples exhibiting larger and more numerous pores corresponding to higher porosity values.

Furthermore, analysis revealed that larger pores exhibited greater deviations from a regular spherical shape, indicating a correlation between pore size and morphological irregularity.

The presence of residual sintering pores and entrapped gas porosity indicates that further reductions in overall porosity could be achieved by optimising the debinding and sintering stages. However, the majority of the total porosity originates from printing-associated defects. Any gaps between deposited layers or other flaws in the green part are carried over into the sintered component because they are too large to close during sintering, ultimately compromising mechanical performance and functionality. These irregular printing-associated pores are particularly detrimental, as their sharp edges create high strain concentrations, increasing the likelihood of crack initiation and mechanical failure. [45,50] Reducing these defects would enable porosity levels comparable to those observed in other additive or conventional manufacturing methods. Strain mapping and fractography analyses further show that printing-related pores are the primary sources of stress concentration and failure initiation. Consequently, minimising large, irregular pores through improved printing process control is essential for achieving reliable mechanical performance.

5. Discussion

Understanding the variability and batch-dependent effects in FFF-manufactured 316L is essential for interpreting the measured mechanical responses and providing guidance for reproducible production. High variability in the measured mechanical responses is largely attributable to the manufacturing process itself, as also reported in previous studies on FFF metal materials [11,12,51]. This variability is inherent to the method, arising from the printing process, which can produce large and irregular defects that affect mechanical behaviour. While printing parameters explain part of the response differences, the stochastic nature of defect formation contributes significantly to the observed scatter in results. In addition, batch-related factors, such as filament storage and moisture content or variations in debinding, sintering, and environmental conditions during printing, can influence the measured properties. Our statistical analysis indicates that including the batch factor is important to account for such variability and highlights that careful consideration of these factors is essential for achieving more consistent and reproducible results in future work.

The highest nozzle temperature of 250° resulted in slightly improved static mechanical properties. This can be attributed to improved filament melting and flow under higher temperatures, leading to more consistent layer adhesion. This finding supports the previously noticed behaviour of filament extrusion manufacturing, where higher nozzle temperatures lead to higher molecular mobility and more efficient interlayer diffusion.[18,20]. However, a small difference in the GRG suggests responses are not highly sensitive to changes in nozzle temperature, as long as it stays in the recommended range.

The highest bed temperature showed better performance both in ANOVA and S/N ratio approach for multiple responses. This suggests that a higher temperature of 120 °C enhances the adhesion of the initial layers, providing a better foundation for printed parts. Another possible explanation is that elevated bed temperatures enhance interlayer bonding strength and improve dimensional accuracy by extending the time available for molecular diffusion before the onset of crystallisation in the polymeric binder part of the filament. In other words, higher bed temperatures slow down cooling, so the material stays in a viscous state, giving polymer chains more time to move and entangle. This leads to better layer adhesion and ultimately better static mechanical properties. Similar conclusions have been reported in multiple research papers dealing with Fused Deposition Modelling (FDM) manufacturing of PLA materials. [20,22,23].

This experiment shows a preference for the greatest print speed. At lower print speeds, filament stays in the nozzle for longer times, which can lead to overheating, degradation, and ultimately oozing and over-extrusion of the material. This can ultimately lead to poor

Table 4.1
Closed porosity measurements based on cross-sectional image analysis.

Sample	Porosity (%)
10.1	1.26
16.2	0.87
11.1	5.42
4.1	1.23
21.1	3.14
3.2	2.38
23.1	2.56
25.1	1.14

layer bonding and defects. Furthermore, these findings support the possibility of excessively slow rates leading to under-fusion from cooling as observed in other research papers dealing with filament extrusion [18,25]. While some studies have observed using slower print speed to improve green-part density and surface quality [21], in 316L metal FFF the optimal speed may vary, especially in combination with nozzle temperatures. When paired with higher nozzle temperatures evident in metal FFF, higher print speeds in metal FFF may enhance material flow while reducing the residence time of the filament in the hot zone and therefore minimising thermal degradation of the polymeric binder. This can help maintain deposition quality and improve overall part integrity.

The preference for smaller layer thickness aligns with findings from previous studies and manufacturer recommendations, indicating improved dimensional accuracy and overall performance [19,26]. These findings support the notion that reducing layer thickness decreases the size of interlayer voids and increases the bonding area between layers [19], therefore enhancing overall material performance.

The lines printing pattern provides more continuous and aligned material paths across layers, promoting stronger interlayer bonding and more efficient stress transfer during loading. While the cubic pattern has been shown to be less anisotropic than other printing patterns, it introduces more discontinuities and frequent changes in direction, which can result in strain concentrations, incomplete bonding at intersections, and a higher likelihood of internal defects.

Infill of 100 % overall showed better and more consistent performance. Over extruding by 5 % might be causing uneven layer height, leading to dimensional inaccuracies and poor mechanical performance.

Fractography analysis showed high porosity of the material caused by a combination of binder removal pores and interlayer defects. Some defects showed smooth and undisturbed surfaces, which suggested non-uniform strain distribution throughout the material. However, certain high-performing specimens showed improved porosity with fewer defects, suggesting that material density and performance can be improved with proper manufacturing process control. Strain mapping showed a correlation between localised strains and defects in the material.

Porosity analysis reveals three main pore types: printing-associated, gas-entrapped, and residual sintering pores. Printing-associated pores dominate, being large, irregular, and aligned with the print direction, and largely persist after sintering, directly impacting mechanical performance. Gas-entrapped pores are small and spherical, while residual sintering pores are partially rounded or irregular. These results indicate that optimising debinding and sintering can reduce small pores, but minimising large printing defects through improved process control is key to achieving lower porosity and reliable mechanical properties.

6. Conclusion

This study investigated the influence of key FFF process parameters on the mechanical performance, dimensional accuracy and failure mechanisms of 316L stainless steel parts produced via metal filament extrusion. The results show that higher values of nozzle and bed temperature, as well as print speed, generally promote stronger interlayer bonding and improve static mechanical response. Lower layer thickness and 100 % infill produced more consistent and dimensionally accurate parts, while line-like pattern showed superior mechanical properties due to better stress distribution and reduced internal defects.

Although the material remains sensitive to porosity arising from printing defects, binder removal and sintering, the findings indicate that proper control of process parameters can significantly reduce defects and enhance part integrity. Fractography and strain analysis confirmed that internal defects strongly correlate with localised strain concentrations and failure mechanisms. Overall, the study highlights the importance of optimising printing conditions to achieve both improved and more predictable performance in 316L stainless steel parts manufactured using metal FFF.

The porosity analysis showed that printing-associated pores are the dominant contributors to total porosity and are primarily responsible for strain concentrations and failure initiation. While gas entrapment and residual sintering pores are present, their effect is secondary. These findings reinforce that controlling printing parameters to minimise large, irregular pores is essential for achieving reliable mechanical performance in metal FFF 316L parts.

The extensive testing and analysis presented here provide systematic insights into the effects of FFF process parameters, while also characterising porosity and defect types and their impact on failure mechanisms, offering practical guidance for optimising printing conditions and predicting part performance.

These findings support the growing potential of low-cost metal additive manufacturing for structural applications, provided that process parameters are carefully selected and controlled. It is also clear that porosity is the leading cause of mechanical material degradation – therefore, a precise control and quantitative assessment of this aspect is of paramount importance for the prediction of material behaviour when FFF of 316L is applied in structural applications.

CRediT authorship contribution statement

J. Zenzerovic: Writing – original draft, Visualization, Validation, Software, Methodology, Formal analysis, Data curation, Conceptualization. **F. Sordetti:** Writing – review & editing, Methodology. **A. Lanzutti:** Writing – review & editing, Methodology. **E. Salvati:** Writing – review & editing, Supervision, Resources, Project administration, Conceptualization.

Declaration of competing interest

The authors declare that they have no known competing financial interests or personal relationships that could have appeared to influence the work reported in this paper.

Acknowledgments

Enrico Salvati would like to acknowledge the European Research Council (ERC) for funding the ERC Starting grant project BREAKDOWN (Grant agreement ID: 101162848).

Appendix A. Additional fractography analysis

Additional fractography analysis was performed on samples with different combinations of infill percentage, line thickness, and infill pattern parameters (Table A1). While these parameters were previously identified as influential for mechanical performance, in this part of the study the intention was not to determine their individual effects on microstructure. Instead, eight samples with comparable average responses were selected based on the expectation that these combinations could produce the greatest variability in microstructural features, allowing for a representative assessment of defect characteristics across different cases.

Table A1
Samples chosen for additional fractography analysis.

Sample number	Infill Pattern	Infill Percentage	Line Thickness
10.1	Lines	100	0.1
16.2	Lines	105	0.1
11.1	Lines	100	0.15
4.1	Lines	105	0.15
21.1	Cubic	100	0.1
3.2	Cubic	105	0.1
23.1	Cubic	100	0.15
25.1	Cubic	105	0.15

All samples showed a consistently high defect rate, in agreement with the initial fractography analysis. The fracture surfaces were dominated by two recurring defect types: large, irregular smooth pores associated with printing-related inconsistencies, and smaller pores attributed to residual porosity from binder removal and sintering.

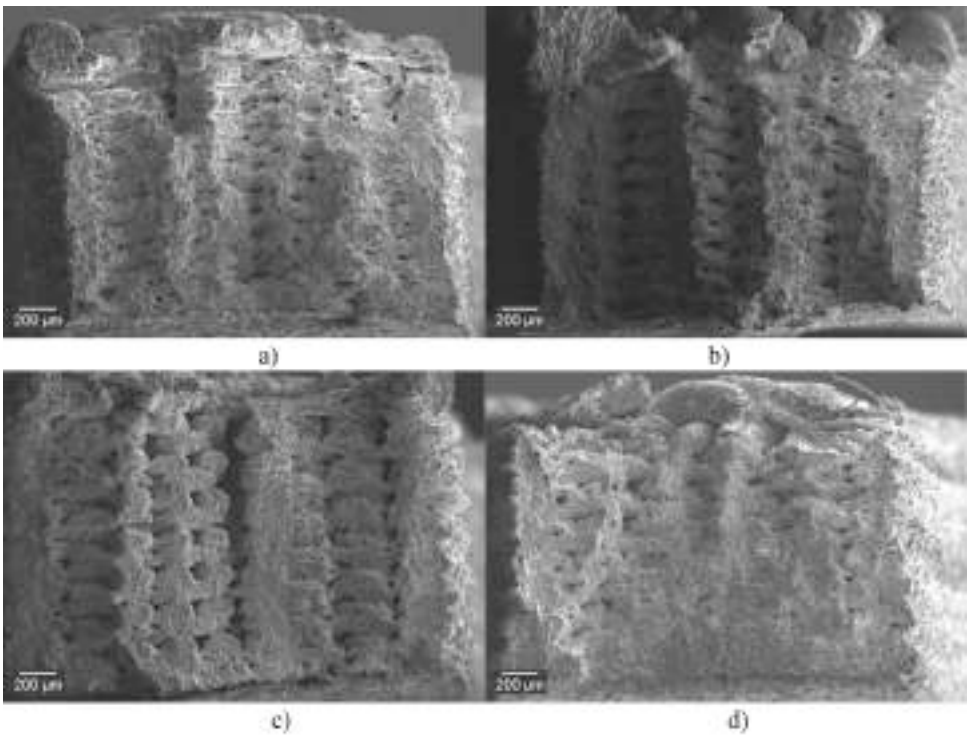

Fig. A1. Fractography analysis for samples with “lines” infill: a) 10.1, b) 16.2, c) 11.1, d) 4.1.

As previously noticed, samples printed with the ‘lines’ infill pattern showed a more predictable defect distribution, with pores occurring vertically and at layer intersections (Fig. A1). In contrast, the ‘cubic’ infill pattern resulted in a more irregular and less predictable distribution of defects, with pores appearing randomly throughout the structure, likely due to the more complex deposition path (Fig. A2).

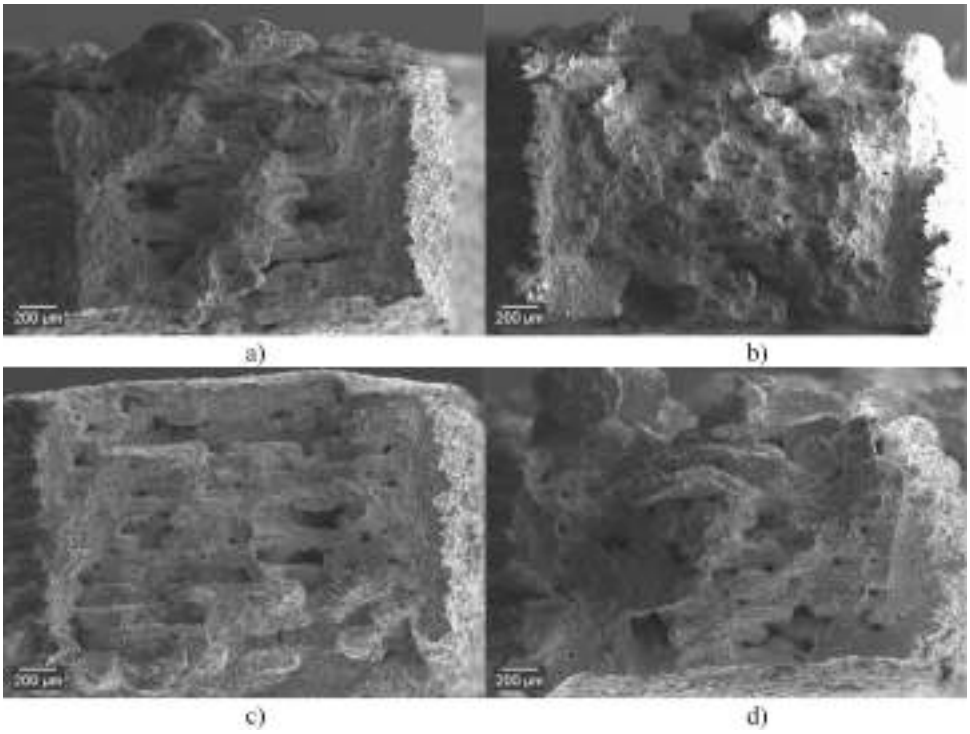

Fig. A2. Fractography analysis for samples with "cubic" infill: a) 21.1, b) 3.2, c) 23.1, d) 25.1.

Data availability

Data will be made available on request.

References

[1] A. Vafadar, F. Guzzomi, A. Rassau, K. Hayward, Advances in metal additive manufacturing: a review of common processes, industrial applications, and current challenges, Appl. Sci. 11 (3) (2021) 1213, https://doi.org/10.3390/app11031213.
[2] J. Jacob, D. Pejak Simunec, A.E.Z. Kandjani, A. Trinchi, A. Sola, A review of fused filament fabrication of metal parts (Metal FFF): current developments and future challenges, Technologies 12 (12) (2024) 267, https://doi.org/10.3390/technologies12120267.
[3] J.M. Costa, E.W. Sequeiros, M.F. Vieira, Fused filament fabrication for metallic materials: a brief review, Materials 16 (24) (2023) 7505, https://doi.org/10.3390/ma16247505.
[4] C. Suwanpreecha, A. Manonukul, A review on material extrusion additive manufacturing of metal and how it compares with metal injection moulding, Metals 12 (3) (2022) 429, https://doi.org/10.3390/met12030429.
[5] Benedict O'Neill, What's the total cost of ownership for metal 3D printing? Accessed: June 16, 2025. [Online]. Available: https://www.aniwaa.com/insight/3d-printers/total-metal-3d-printing-cost/.
[6] N. Khanna, H. Salvi, B. Karaş, I. Fairoz, A. Shokrani, Cost modelling for powder bed fusion and directed energy deposition additive manufacturing, J. Manuf. Mater. Process. 8 (4) (2024) 142, https://doi.org/10.3390/jmmp8040142.
[7] P. Parenti, D. Puccio, Q. Semeraro, B.M. Colosimo, A techno-economic approach for decision-making in metal additive manufacturing: metal extrusion versus single and multiple laser powder bed fusion, Prog. Addit. Manuf. 9 (2) (2024) 185–210, https://doi.org/10.1007/s40964-023-00442-7.
[8] N.K. Bankapalli, V. Gupta, P. Saxena, A. Bajpai, C. Lahoda, J. Polte, Filament fabrication and subsequent additive manufacturing, debinding, and sintering for extrusion-based metal additive manufacturing and their applications: a review, Compos. Part B Eng. 264 (2023) 110915, https://doi.org/10.1016/j.compositesb.2023.110915.
[9] Z. Lotfizarei, A. Mostafapour, A. Barari, A. Jalili, A.E. Patterson, Overview of debinding methods for parts manufactured using powder material extrusion, Addit. Manuf. 61 (2023) 103335, https://doi.org/10.1016/j.addma.2022.103335.
[10] M.C. Brennan, J.S. Keist, T.A. Palmer, Defects in metal additive manufacturing processes, J. Mater. Eng. Perform. 30 (7) (2021) 4808–4818, https://doi.org/10.1007/s11665-021-05919-6.
[11] C. Wang, W. Mai, Q. Shi, Z. Liu, Q. Pan, J. Peng, Effect of printing parameters on mechanical properties and dimensional accuracy of 316L stainless steel fabricated by fused filament fabrication, J. Mater. Eng. Perform. 33 (21) (2024) 11781–11793, https://doi.org/10.1007/s11665-023-08848-8.
[12] S. Spiller, S.O. Kolstad, N. Razavi, Fabrication and characterization of 316L stainless steel components printed with material extrusion additive manufacturing, Procedia Struct. Integr. 42 (2022) 1239–1248, https://doi.org/10.1016/j.prostr.2022.12.158.
[13] Y. Zhang, S. Bai, M. Riede, E. Garratt, A. Roch, A comprehensive study on fused filament fabrication of Ti-6Al-4V structures, Addit. Manuf. 34 (2020) 101256, https://doi.org/10.1016/j.addma.2020.101256.
[14] M. Carminati, G. D'Urso, C. Giardini, The enhancement of mechanical properties via post-heat treatments of AISI 630 parts printed with material extrusion, Prog. Addit. Manuf. 8 (6) (2023) 1341–1355, https://doi.org/10.1007/s40964-023-00401-2.
[15] M.Á. Caminero, A. Romero, J.M. Chacón, P.J. Núñez, E. García-Plaza, G.P. Rodríguez, Additive manufacturing of 316L stainless-steel structures using fused filament fabrication technology: mechanical and geometric properties, Rapid Prototyp. J. 27 (3) (2021) 583–591, https://doi.org/10.1108/RPJ-06-2020-0120.

[16] S.O. Obadimu, A. Kasha, K.I. Kourousis, Tensile performance and plastic anisotropy of material extrusion steel 316L: Influence of primary manufacturing parameters, Addit. Manuf. 60 (2022) 103297, https://doi.org/10.1016/j.addma.2022.103297.
[17] Y. Tao, et al., A review on voids of 3D printed parts by fused filament fabrication, J. Mater. Res. Technol. 15 (2021) 4860–4879, https://doi.org/10.1016/j.jmrt.2021.10.108.
[18] G. Gao, F. Xu, J. Xu, G. Tang, Z. Liu, A Survey of the influence of process parameters on mechanical properties of fused deposition modeling parts, Micromachines 13 (4) (2022) 553, https://doi.org/10.3390/mi13040553.
[19] T. Gajjar, R. Yang, L. Ye, Y.X. Zhang, Effects of key process parameters on tensile properties and interlayer bonding behavior of 3D printed PLA using fused filament fabrication, Prog. Addit. Manuf. 10 (2) (2025) 1261–1280, https://doi.org/10.1007/s40964-024-00704-y.
[20] S. Liparoti, D. Sofia, A. Romano, F. Marra, R. Pantani, Fused filament deposition of PLA: the role of interlayer adhesion in the mechanical performances, Polymers 13 (3) (2021) 399, https://doi.org/10.3390/polym13030399.
[21] H. O'Connor, G. Singh, A. Kumar, R. Paetzold, M. Celikin, E.D. O'Cearbhaill, Fused filament fabrication using stainless steel 316L -polymer blend: Analysis and optimization for green density and surface roughness, Polym. Compos. 45 (12) (2024) 10632–10644, https://doi.org/10.1002/pc.28496.
[22] C. Benwood, A. Anstey, J. Andrzejewski, M. Misra, A.K. Mohanty, Improving the impact strength and heat resistance of 3D printed models: structure, property, and processing correlationships during fused deposition modeling (FDM) of poly(lactic Acid), ACS Omega 3 (4) (2018) 4400–4411, https://doi.org/10.1021/acsomega.8b00129.
[23] M.R. Caputo, et al., Influence of FFF process conditions on the thermal, mechanical, and rheological properties of poly(hydroxybutyrate-co-hydroxy hexanoate), Polymers 15 (8) (2023) 1817, https://doi.org/10.3390/polym15081817.
[24] Y. Zhang, K. Chou, A parametric study of part distortions in fused deposition modelling using three-dimensional finite element analysis, Proc. Inst. Mech. Eng. Part B J. Eng. Manuf. 222 (8) (2008) 959–968, https://doi.org/10.1243/09544054JEM990.
[25] M. Faes, E. Ferraris, D. Moens, Influence of inter-layer cooling time on the quasi-static properties of ABS components produced via fused deposition modelling, Procedia CIRP 42 (2016) 748–753, https://doi.org/10.1016/j.procir.2016.02.313.
[26] O. Iyibilgin, Investigation of the effect of layer thickness on the mechanical properties of 316L austenitic stainless steel in additive manufacturing with metal filament, Appl. Sci. 15 (5) (2025) 2584, https://doi.org/10.3390/app15052584.
[27] A. Pellegrini, M.E. Palmieri, M.G. Guerra, Evaluation of anisotropic mechanical behaviour of 316L parts realized by metal fused filament fabrication using digital image correlation, Int. J. Adv. Manuf. Technol. 120 (11–12) (2022) 7951–7965, https://doi.org/10.1007/s00170-022-09303-z.
[28] J. Damon, S. Dietrich, S. Gorantla, U. Popp, B. Okolo, V. Schulze, Process porosity and mechanical performance of fused filament fabricated 316L stainless steel, Rapid Prototyp. J. 25 (7) (2019) 1319–1327, https://doi.org/10.1108/RPJ-01-2019-0002.
[29] V. Di Pompeo, E. Santecchia, A. Santoni, K. Sleem, M. Cabibbo, S. Spigarelli, Microstructure and defect Analysis of 17-4PH stainless steel fabricated by the bound metal deposition additive manufacturing technology, Crystals 13 (9) (2023) 1312, https://doi.org/10.3390/cryst13091312.
[30] P. Schüßler, et al., Characterization of the metal fused filament fabrication process for manufacturing of pure copper inductors, Materials 16 (20) (2023) 6678, https://doi.org/10.3390/ma16206678.
[31] N. Kurgan, Effect of porosity and density on the mechanical and microstructural properties of sintered 316L stainless steel implant materials, Mater. Des. 55 (2014) 235–241, https://doi.org/10.1016/j.matdes.2013.09.058.
[32] R.M. German, Sintering: from Empirical Observations to Scientific Principles, 1st. ed., Elsevier/Butterworth-Heinemann, Amsterdam, 2014.
[33] Y. Lee, P. Nandwana, S. Simunovic, Powder spreading, densification, and part deformation in binder jetting additive manufacturing, Prog. Addit. Manuf. 7 (1) (2022) 111–125, https://doi.org/10.1007/s40964-021-00214-1.
[34] A. Zavaliangos, J.M. Missiaen, D. Bouvard, Anisotropy in shrinkage during sintering, Sci. Sinter. 38 (1) (2006) 13–25, https://doi.org/10.2298/SOS0601013Z.
[35] Standard Specification for Chromium and Chromium-Nickel Stainless Steel Plate, Sheet, and Strip for Pressure Vessels and for General Applications, Jan. 05, 2022.
[36] BASF, Ultrafuse 316L Technical Data Sheet. Accessed: June 17, 2025. [Online]. Available: https://forward-am.com/wp-content/uploads/2021/01/Ultrafuse_316L_TDS_EN_v1.1.pdf.
[37] F.A. BASF, Ultrafuse 316L Process Instructions. Accessed: June 17, 2025. [Online]. Available: https://forward-am.com/wp-content/uploads/2021/01/Process-Guidelines-Ultrafuse-316L.pdf.
[38] E. Jones et al., A Good Practices Guide for Digital Image Correlation, International Digital Image Correlation Society, Oct. 2018. https://doi.org/10.32720/idics/gpg.ed1/print.format.
[39] H. Schreier, J.-J. Orteu, M.A. Sutton, Image Correlation for Shape, Motion and Deformation Measurements: Basic Concepts, Theory and Applications, Springer US, Boston, MA, 2009. https://doi.org/10.1007/978-0-387-78747-3.
[40] E28 Committee, Test Methods for Rockwell Hardness of Metallic Materials. https://doi.org/10.1520/E0018-22.
[41] J. Jansa, et al., Corrosion and material properties of 316L stainless steel produced by material extrusion technology, J. Manuf. Process. 88 (2023) 232–245, https://doi.org/10.1016/j.jmapro.2023.01.035.
[42] X. Kan, D. Yang, Z. Zhao, J. Sun, 316L FFF binder development and debinding optimization, Mater. Res. Express 8 (11) (2021) 116515, https://doi.org/10.1088/2053-1591/ac3b15.
[43] J. Gonzalez-Gutierrez, S. Cano, S. Schuschnigg, C. Kukla, J. Sapkota, C. Holzer, Additive manufacturing of metallic and ceramic components by the material extrusion of highly-filled polymers: a review and future perspectives, Materials 11 (5) (2018) 840, https://doi.org/10.3390/ma11050840.
[44] K. Pan, et al., Formation and evolution mechanisms of micropores in powder metallurgy Ti alloys, Mater. Des. 223 (2022) 111202, https://doi.org/10.1016/j.matdes.2022.111202.
[45] N. Chawla, X. Deng, Microstructure and mechanical behavior of porous sintered steels, Mater. Sci. Eng. A 390 (1–2) (2005) 98–112, https://doi.org/10.1016/j.msea.2004.08.046.
[46] N. Kurgan, Y. Sun, B. Cicek, H. Ahlatci, Production of 316L stainless steel implant materials by powder metallurgy and investigation of their wear properties, Chin. Sci. Bull. 57 (15) (2012) 1873–1878, https://doi.org/10.1007/s11434-012-5022-5.
[47] R. Bjørk, H.L. Frandsen, N. Pryds, Modeling the microstructural evolution during constrained sintering, J. Am. Ceram. Soc. 98 (11) (2015) 3490–3495, https://doi.org/10.1111/jace.13701.
[48] S. You, D. Jiang, F. Wang, F. Ning, Anisotropic sintering shrinkage behavior of stainless steel fabricated by extrusion-based metal additive manufacturing, J. Manuf. Process. 101 (2023) 1508–1520, https://doi.org/10.1016/j.jmapro.2023.07.026.
[49] M.A. Wagner, et al., Filament extrusion-based additive manufacturing of 316L stainless steel: Effects of sintering conditions on the microstructure and mechanical properties, Addit. Manuf. 59 (2022) 103147, https://doi.org/10.1016/j.addma.2022.103147.
[50] N.T. Aboulkhair, M. Simonelli, L. Parry, I. Ashcroft, C. Tuck, R. Hague, 3D printing of aluminium alloys: additive manufacturing of aluminium alloys using selective laser melting, Prog. Mater Sci. 106 (2019) 100578, https://doi.org/10.1016/j.pmatsci.2019.100578.
[51] S. Kedziora, et al., Strength properties of 316L and 17-4 PH stainless steel produced with additive manufacturing, Materials 15 (18) (2022) 6278, https://doi.org/10.3390/ma15186278.